

Night-time Ionospheric Localized Enhancements (NILE) Observed in North America Following Geomagnetic Disturbances

A.T. Chartier¹, S. Datta-Barua², S. McDonald³, G.S. Bust¹, J. Tate⁴, L.P. Goncharenko⁵, G. Romeo¹, R. Schaefer¹,

¹ Johns Hopkins Applied Physics Laboratory

² Illinois Institute of Technology

³ Naval Research Laboratory

⁴ Computational Physics, Inc.

⁵ MIT Haystack Observatory

Abstract

The Ionospheric Data Assimilation Four-Dimensional (IDA4D) technique has been coupled to Sami3 is Another Model of the Ionosphere (SAMI3). In this application, ground- and space-based GPS Total Electron Content (TEC) data have been assimilated into SAMI3, while *in situ* electron densities, autoscaled ionosonde NmF2 and reference GPS stations have been used for validation. IDA4D/SAMI3 shows that Night-time Ionospheric Localized Enhancements (NILE) are formed following geomagnetic storms in November 2003 and August 2018. The NILE phenomenon appears as a moderate, longitudinally extended enhancement of NmF2 at 30-40° N MLAT, occurring in the late evening (20-24 LT) following much larger enhancements of the equatorial anomaly crests in the main phase of the storms. The NILE appears to be caused by upward and northward plasma transport around the dusk terminator, which is consistent with eastward polarization electric fields. Independent validation confirms the presence of the NILE, and indicates that IDA4D is effective in correcting random errors and systematic biases in SAMI3. In all cases, biases and root-mean-square errors are reduced by the data assimilation, typically by a factor of 2 or more. During the most severe part of the November 2003 storm, the uncorrected ionospheric error on a GPS 3D position at 1LSU (Louisiana) is estimated to exceed 34 m. The IDA4D/SAMI3 specification is effective in correcting this down to 10-m.

Key points

The IDA4D data assimilation scheme has been coupled to the SAMI3 ionospheric model

IDA4D/SAMI3 shows Night-time Ionospheric Localized Enhancements (NILE) at midlatitudes after storms

Formation of the NILE appears to be caused by upward/northward plasma transport near the dusk terminator

1. Introduction

1. 1 Past observations

Nighttime Ionospheric Localized Enhancements (NILE) have been observed at northern mid-latitudes during the recovery phase of major storms and superstorms (Datta-Barua, 2004; Datta-Barua et al., 2008), notably 31 October and 20 November 2003. The NILE constitutes a major enhancement of the ionosphere relative to the background nighttime ionosphere, in a latitudinally narrow channel extending from the south-east to the northwest. In all cases observed to date, the NILE appears to originate above the Caribbean and extends into the continental USA. This phenomenon is not currently understood.

1. 2 NILE in the context of storm-time dynamics

The ionospheric effects of geomagnetic storms have received a great deal of scientific attention. Prölss' (2008) review of midlatitude storm effects highlights the fact that many storm effects related to winds and electric field are not well understood or comprehensively observed. However, there are some stormtime phenomena that are relatively well-known, and the NILE should be considered within the context of these. Rishbeth (1975) and Buonsanto (1999) provide reviews of these effects. During active magnetic periods, electric fields arise at all latitudes from at least two sources. The first are the "prompt penetration" electric fields of magnetospheric origin that arise due to variations in the Region 1 and Region 2 field-aligned current systems (observed e.g. by Kelley et al., 1979; modeled by Huba et al., 2005). The second are the "disturbance dynamo" fields driven by thermospheric winds (themselves driven by high-latitude magnetospheric energy deposition) acting on the ionospheric plasma (Blanc and Richmond, 1980). Prompt penetration electric fields are believed to be responsible for increases in the density of the equatorial ionization anomaly, up to 330 TECU in the Halloween 2003 case shown by Mannucci et al. (2005). Tsurutani et al. (2008) explained this effect as a "superfountain," where the equatorial fountain effect is greatly enhanced leading to uplifts of density that can last several hours. Huba and Sazykin (2014) presented model results that linked this low-latitude storm effect to the formation of mid-latitude Storm-Enhanced Density regions (SEDs). Another well-known storm effect that occurs at midlatitudes is the "negative phase" during which thermospheric composition changes suppress plasma levels by increasing recombination rates (observed by Tausch, 1971; simulated by Fuller-Rowell, 1998). This negative phase typically follows the positive storm effects driven by winds and magnetospheric electric fields. More recently, the effect of electric fields at the solar terminator has been suggested to cause important midlatitude ionospheric effects during storms. Foster and Erickson (2013) point to the important role of the "polarization terminator" in generating enhanced disturbance time TEC at lower middle latitudes, convected upward/poleward from the EIA. The conductivity gradient along the solar terminator creates eastward electric fields, which lead to upward ExB plasma motion at the dip equator, and upward/poleward ExB motion in the northern hemisphere. The authors point to a preferred longitude/UT sector for this effect, which is around 21 UT in the western Atlantic.

State-of-the-art physics models account for many important electrodynamic and chemical effects, and have been shown to be able to model the SED. However global models have not, to date, captured the localized nature of the NILE. We seek to address the improvement in modeling the plasma density of the NILE using data assimilation.

1. 3 Outstanding questions related to the NILE effect

This analysis of the NILE effect leads to several questions, notably: What is the spatial extent of the NILE, and what causes it? Does the NILE also occur in less-intense periods of geomagnetic disturbance? Can the effect be validated using data other than GPS-derived TEC?

2. Method

2. 1 Summary of the method

This investigation uses assimilation of GPS-derived TEC data (the IDA4D technique) to correct a first-principles ionospheric model (SAMI3) in order to produce three-dimensional, time-dependent images of electron density during two ionospheric storms. The primary case is 20-21 November 2003, which is the most recent ionospheric superstorm. The storm of 25 – 26 August 2018 is chosen as a comparison case because it has good data coverage and covers a moderately intense geomagnetic disturbance. For validation, we use independent GPS stations, ionosonde data and *in situ* density data from the CHAMP and Swarm satellites.

2. 2 Solar/geomagnetic indices during the two cases

IMF Bz, Kp and F10.7 for the two cases (November 2003 and August 2018) are shown in Figure 1. Following Loewe and Prolss (1997) these events classify as a great storm (Dst= -422 nT at 20-21 UT on 20 November 2003), and a strong storm (Dst= -174 nT at 6-7 UT on 26 August 2018). Ambient levels of ionization are also likely to be substantially different due to the variations in Solar flux (F10.7=171 on 20 November 2003 vs 73 on 25 August 2018).

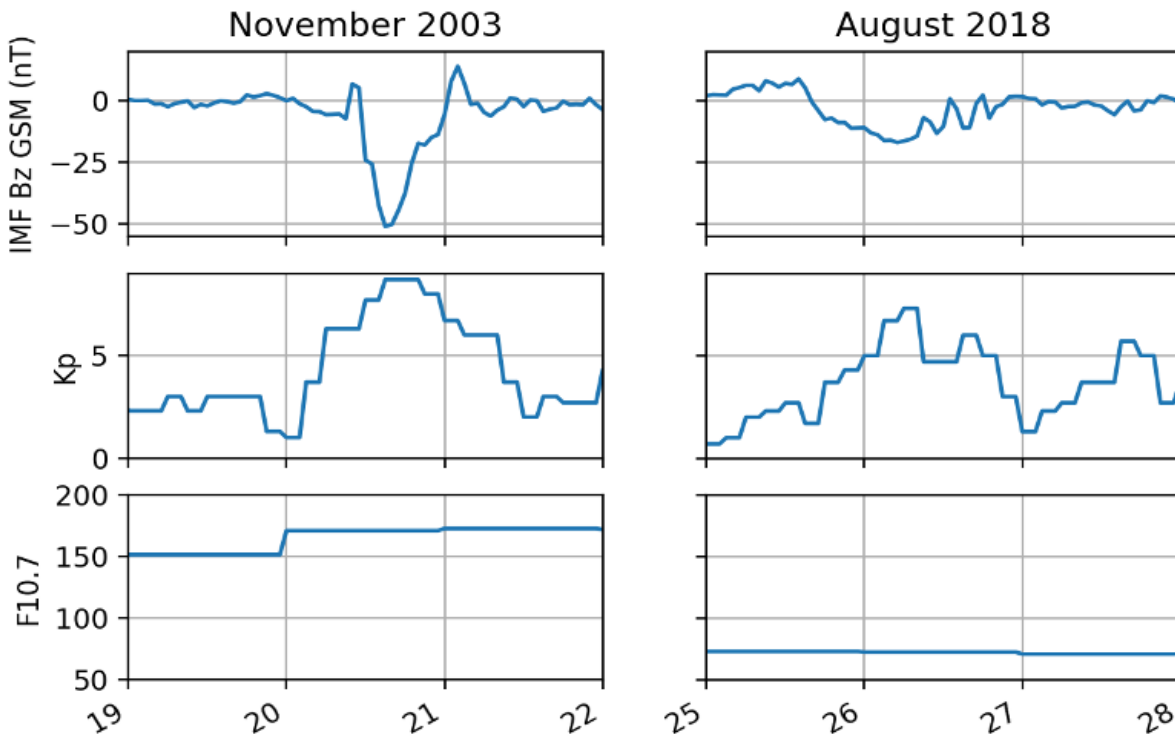


Figure 1 shows IMF Bz (propagated to the bow shock in GSM coordinates), Planetary K-index (Kp) and 10.7 cm Solar flux index (F10.7) for the two case studies selected here (November 19-22 2003 and August 25-28 2018).

2.3 Ionospheric data assimilation

The IDA4D technique is used to assimilate ionospheric observations into the SAMI3 model, updating its electron and ion density distributions. The model then advances five minutes in time, before the next update is performed.

IDA4D (by Bust et al., 2004) uses a Gauss-Markov Kalman filter to update the prior electron density state, with the model errors based on a dynamically-evolving variance and a heuristic set of correlations that vary according to geomagnetic activity, latitude and time of day. Data assimilation updates are performed at a five-minute cadence. The assimilation scheme can handle multiple data-types, but in this application we use only GPS data from ground stations (~4000 in 2018, ~1500 in 2003), supplemented by CHAMP and GRACE satellite GPS data in the 2003 case. IDA4D runs on a latitude-longitude-altitude grid while SAMI3 uses a geomagnetic field-aligned grid, so interpolation routines are required to couple them together. The Earth System Modeling Framework (ESMF) by Collins et al. (2005) is used for that purpose. As an example, five minutes of assimilation data for the 2003 and 2018 cases are shown in Figure 2.

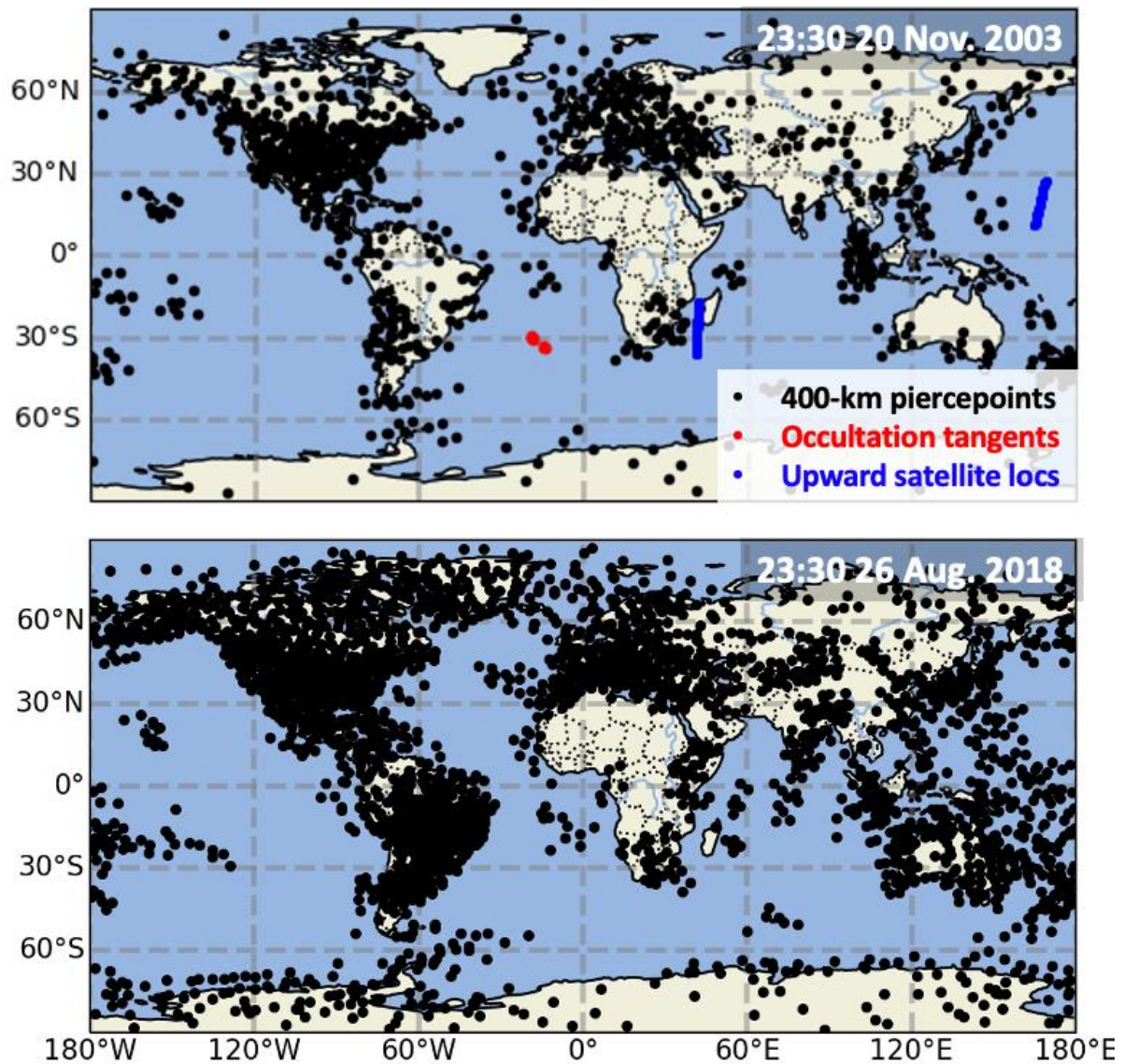


Figure 2 shows the data assimilated in a single five-minute assimilation step centered on 23:30 UT on 20 November 2003 and 26 August 2018. The 400-km piercepoints of ground-to-space GPS TEC data are in black. Tangent points of radio occultation data are in red. Locations of satellites taking upward GPS TEC measurements are in blue.

SAMI3 (by Huba et al., 2000; 2008) solves for the dynamic plasma and chemical evolution of seven ion species (H^+ , He^+ , N_2^+ , O^+ , N^+ , NO^+ , and O_2^+) on a field-aligned magnetic apex coordinate grid extending up to 87° MLAT (Richmond, 1995). Photoionization is calculated using solar flux from the Flare Irradiance Spectral Model by Chamberlin et al. (2008), which is driven by Solar Dynamics Observatory Extreme Ultraviolet Variability Experiment data. SAMI3 contains a self-consistent electric potential solver that is

seamlessly combined with an imposed high-latitude potential from Weimer's (2005) model (driven by solar wind parameters observed by the Advanced Composition Explorer), though the model does not yet account for polarization electric fields. The Hardy model (Hardy et al., 1985, 1989) provides auroral electron and ion precipitation estimates based on the K_p index. The neutral atmosphere is specified by the Horizontal Wind Model 2014 by Drob et al. (2015) and the Naval Research Laboratory's Mass Spectrometer Incoherent Scatter Model 2000 of neutral atmospheric densities by Picone et al. (2002).

2.4 Validation using GPS data

Since ionospheric electron density enhancements can have a major impact on GPS positioning, it is useful to consider model performance in correcting 3D position estimates at test receiver stations shown in Figure 3.

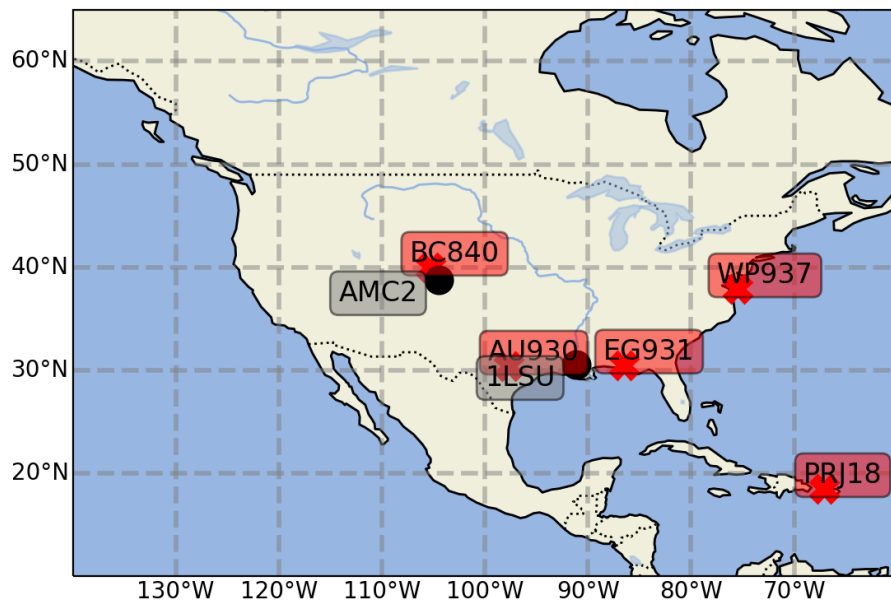


Figure 3: GPS (in black) and Digisonde (in red) stations used for validation of model output.

This is achieved as follows:

First, the ionospheric range error on single-frequency GPS is calculated based on the dual-frequency TEC data observed by the reference GPS stations. Second, a correction is applied based on the model (either IDA4D/SAMI3 or SAMI3). Finally an inversion is performed to estimate the 3D position of the test receivers, based on the observed ionospheric delays and the modeled corrections. This is compared against the known true position of the test receivers.

The observed range, d_{obs} , is calculated by adding the true distance between the i^{th} satellite position, \mathbf{x}_i , based on precise orbit files) and receiver, \mathbf{d}_{true} , and the delay due to slant Total Electron Content (sTEC) between the satellite and receiver, d_{iono} . At L1 (1575.42 MHz), the following applies:

where $sTEC$ is in TEC units (10^{16} el. m^{-3}) and d_{iono} is in meters. From these simulated ranges, the single-frequency position estimate, \mathbf{rx}_{est} , can be obtained by minimizing a cost function. In that cost function, the satellite's elevation angle, e , is used as a scaling factor to prioritize fitting to satellites overhead rather than at low angles, where ionospheric and other errors are typically much larger:

$$\mathbf{rx}_{est} = arg.min. \sum_i ((\mathbf{rx} - \mathbf{tx}_i)^2 - d_{obs_i}^2)^2 \cdot e \quad (2)$$

Following estimation of \mathbf{rx}_{est} using Equation 2, the 3D position error is calculated as the distance between \mathbf{rx}_{est} and the known true position of the receiver. Assimilation schemes that ingest GPS data, such as IDA4D, might be expected to perform well in this type of test because of the potential for common biases inherent to GPS data. Therefore it is important that the model output is also compared to data from other types of instrument.

2.5 Validation using ionosonde data

Predictions of peak density (NmF2) from the first-principles model (SAMI3) and the coupled SAMI3/IDA4D are compared to independent data from the Digisonde network of ionosondes. The Digisonde parameters are based on autoscaled ionograms, as obtained from the Digital Ionogram Database (DIDBase) maintained by UMass Lowell. The autoscaling software is the Automatic Real Time Ionogram Scaling Technique (ARTIST), presented by Galkin et al. (2008). Ionogram autoscaling techniques have well-known limitations, especially during periods of geomagnetic disturbance (as described for example by Ippolito et al., 2018). Nevertheless, autoscaled ionosonde data represents the only independent means of validating global ionospheric models that ingest GNSS data – no other instrument class has comparable spatio-temporal coverage. The peak electron density (NmF2) is the most reliable ionosonde parameter, and although the DIDBase also contains other parameters of interest (e.g. hmF2) we were unable to confirm their accuracy and so they are not used here.

2.6 Validation using CHAMP and Swarm data

Polar-orbiting satellites provide an advantage over ground-based observatories in that they have truly global coverage. This feature of the CHAMP and Swarm satellites' *in situ* density dataset is used to validate the model in cases where the phenomena of interest are present over the oceans. CHAMP (described by Reigber, 2002) was in an orbit of 87.2° inclination at ~ 455 km in November 2003, and operated from 2000 – 2010. Swarm A is in an 87.4° orbit < 460 km and has been flying since 22 November 2013. The Swarm mission is described by Friis-Christensen et al. (2008).

3. Results

3.1 November 2003 storm

The evolution of the November 2003 storm, as captured by IDA4D/SAMI3, is shown in Figure 4. This data shows an enormous enhancement of NmF2 up to $2E13$ el. m^{-3} at 21 UT.

Note that this enhancement occurs much later in local time than might be expected, covering the region approximately 0-80 W (16-24 LT).

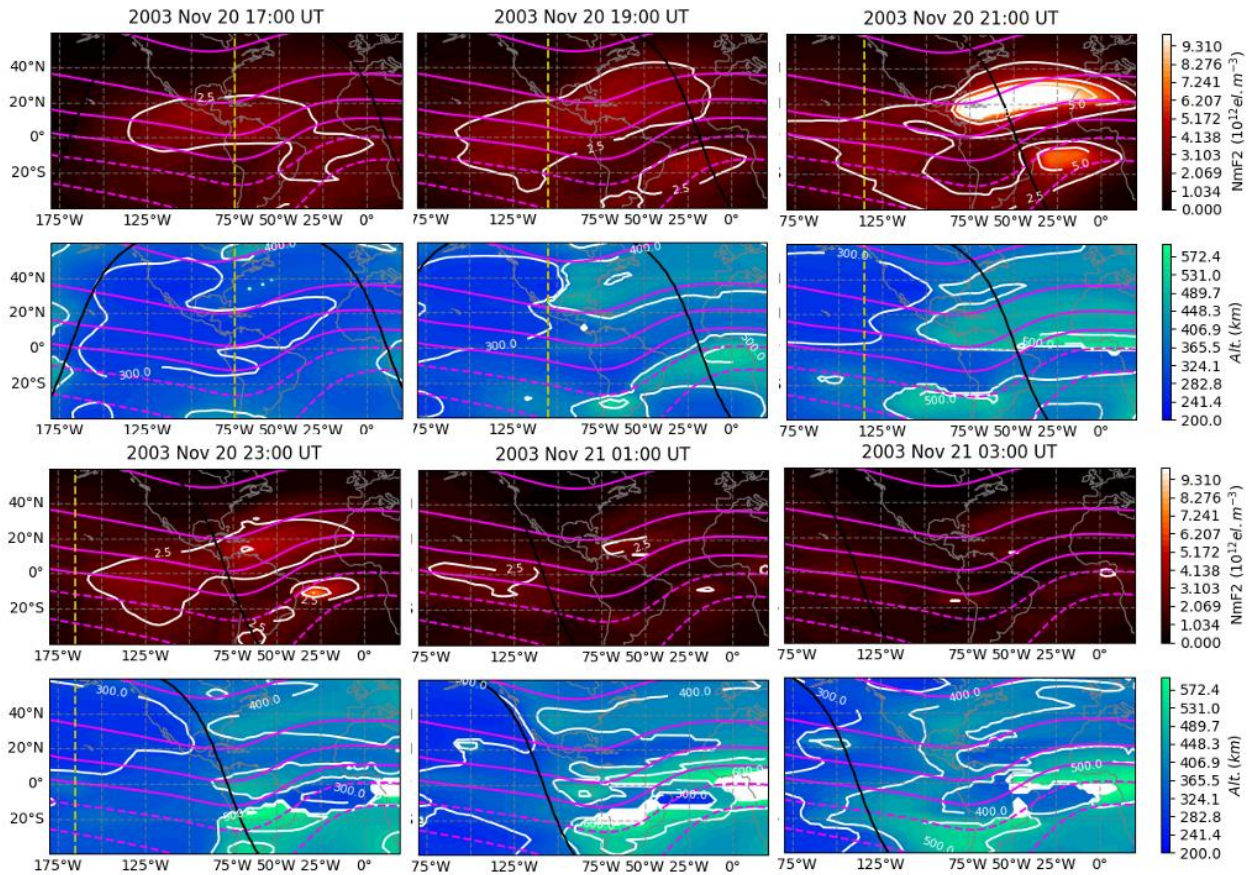


Figure 4: Evolution of the November 2003 storm as captured by IDA4D/SAMI3. NmF2 above in red/yellow, hmF2 below in blue/green (saturated parts are white). NmF2 contours are spaced by 2.5×10^{12} el. m^{-3} (starting at 2×10^{12} el. m^{-3}) while hmF2 contours are spaced by 125 km of altitude. Panels cover 18:30 – 23:30 UT at hourly intervals. Local noon is shown as a yellow dashed line.

IDA4D/SAMI3 indicates a huge enhancement of the equatorial ionization anomaly in the late evening sector, peaking at 2×10^{12} el. m^{-3} at 21:00 UT. The density enhancement is accompanied by a dramatic uplift of the ionospheric peak height close to the equator (between the anomaly crests). At 21:30 UT (not shown) the peak height in that region reaches 711 km. This supercharging of the “fountain” effect is responsible for the enhanced NmF2 poleward of the uplift region. The northern enhanced EIA crest remains visible for >5 hours, effectively “stuck” above the Caribbean with a peak around 70° W.

The IDA4D/SAMI3 model output shown in Figure 5 focuses on the NILE in the night following the November 2003 storm. These snapshots show the NILE as a ridgelike enhancement around 30° N, extending East from ~75° West. The NILE ridge appears to form out of the decaying northern anomaly crest.

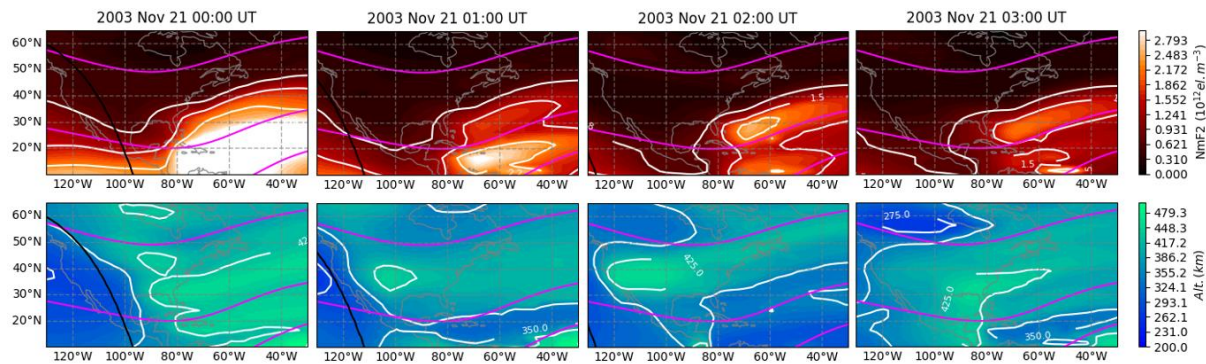


Figure 5: Night-time ionospheric localized enhancements (NILE) in the American sector following the November 2003 storm, as estimated by IDA4D/SAMI3. Upper: NmF2 in red/yellow, lower: hmF2 in blue/green. International Geomagnetic Reference Field inclination contours are shown in magenta.

3.2 August 2018 storm

By comparison to November 2003, the August 2018 storm effects are much smaller in magnitude. Figure 6 shows the evolution of the storm. Note that the color extents are reduced compared to Figure 4 (NmF2 goes to 1.8×10^{12} vs 1×10^{13} el. m^{-3} , hmF2 goes to 500 vs 600 km), and the storm occurs somewhat later in UT.

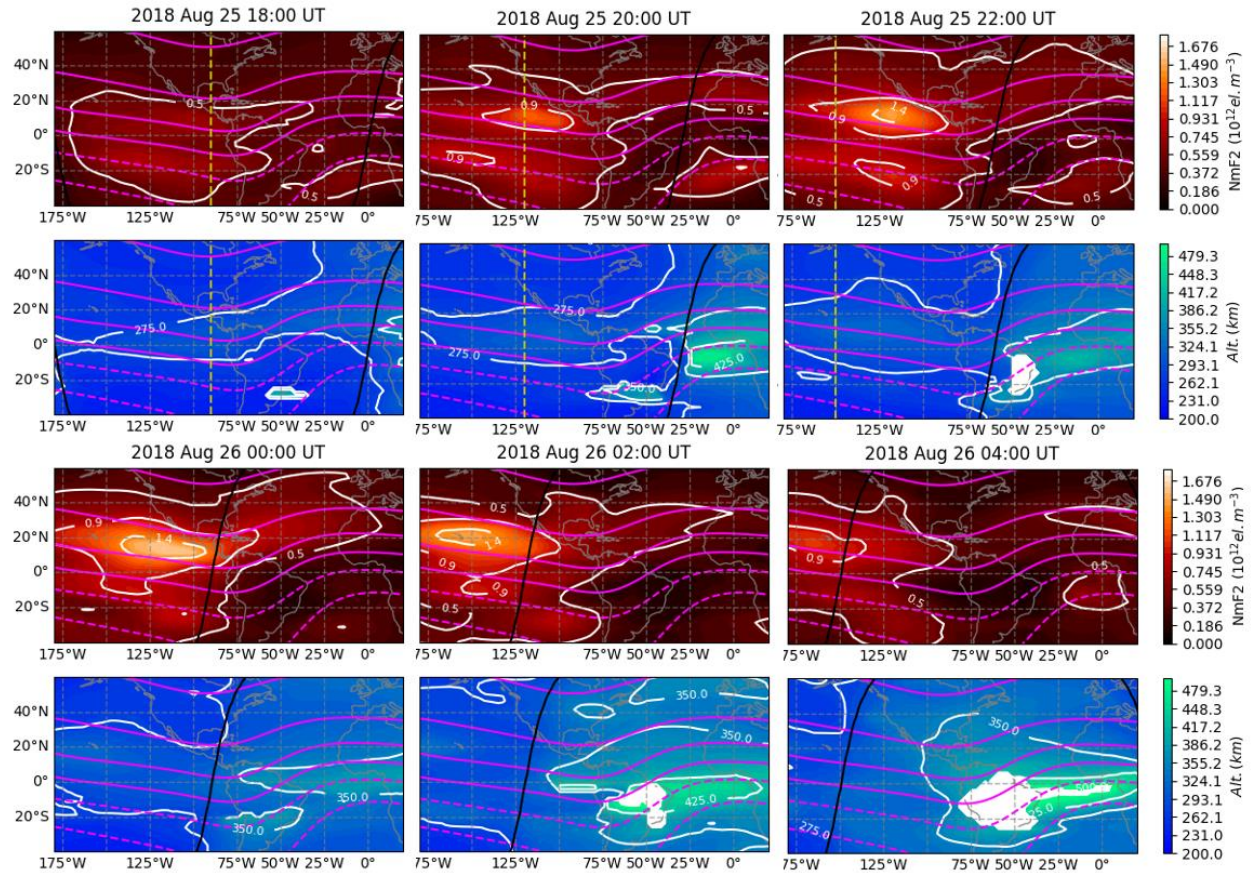


Figure 6: Evolution of the 25-26 August 2018 storm as captured by IDA4D/SAMI3. NmF2 above in red/yellow, hmF2 below in blue/green (saturated sections shown in white). NmF2 contours are spaced by 4×10^{12} el. m^{-3} (starting at 2×10^{12} el. m^{-3}) while hmF2 contours are spaced by 75 km of altitude. Panels cover 20:30 – 01:30 UT at hourly intervals. Local noon is shown as a yellow dashed line.

236

237 As in November 2003, the storm shows an enhancement of the equatorial ionization
 238 anomaly post-noon, which appears to be caused by a plasma uplift between the crests.
 239 Once again, the northern EIA crest is more strongly enhanced than the southern crest.
 240 Unlike November 2003, however, the enhancement moves westward over the course of the
 241 six hours shown in the plots.

242

243 There is a localized night-time enhancement following the August 2018 storm. This feature
 244 occurs over the central USA. This enhancement, shown in Figure 7, is smaller (in both
 245 relative and absolute terms) than the one on 21 November 2003, but better observational
 246 coverage in 2018 as compared to 2003 means this storm can be imaged more completely.
 247 Both enhancements extend along lines of approximately constant geomagnetic latitude,
 248 though the August event is approximately 10 degrees higher in latitude. The August 2018
 249 enhancement is further west than the November 2003 enhancement, consistent with the

different UTs of the two storm onsets (Dst reaches a minimum at 6-7 UT on 26 August 2018, versus 20-21 UT on 20 November 2003). The night-time enhancement “blob” over the USA at 3 UT is clearly formed of plasma originating in the tail of the northern EIA crest. This plasma appears to be lifted to higher latitudes along the line of the terminator.

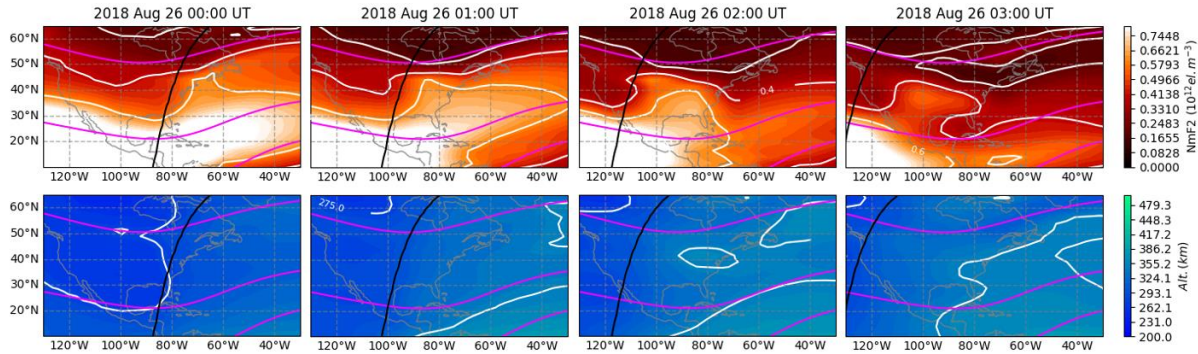


Figure 7: Night-time ionospheric localized enhancements (NILE) in the American sector following the August 2018 storm, as estimated by IDA4D/SAMI3. Upper: NmF2 in red/yellow, lower: hmF2 in blue/green. International Geomagnetic Reference Field inclination contours are shown in magenta.

3.3 Validation using *in situ* data

The CHAMP *in situ* density dataset allows for direct validation of the NILE phenomenon seen around 3:00 UT on 20 November 2003 (shown in Figure 5). Data from CHAMP’s successor, Swarm, are available to validate the August 2018 case, though the relevant pass is too early to see the NILE on that day. Note that these data are not used by IDA4D in this case, so the output in Figure 8 is an independent validation. On 21 November 2003, CHAMP passed approximately along the 60°W meridian at 455 km altitude, moving from south to north between 2:25 and 3:00 UT. The NILE enhancement around 30°N is clearly visible in CHAMP and in IDA4D/SAMI3, as are the other major features of both plots – notably the northern EIA crest around 15°N and the southern crest between 35–50°S. These features are either absent or distorted in the standalone SAMI3 output. In the August 2018 case, IDA4D/SAMI3 also greatly improves agreement between model and data.

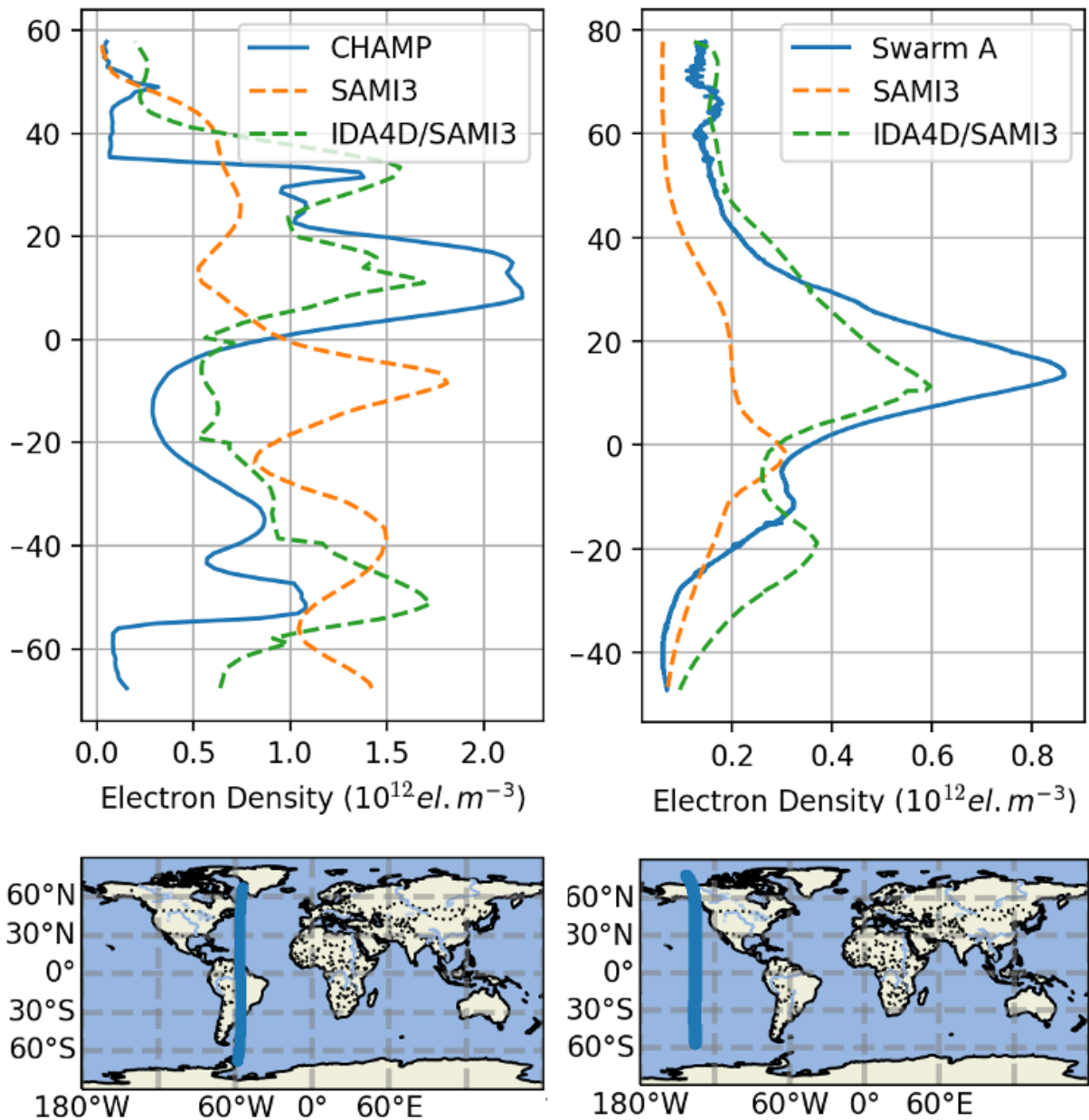


Figure 8: Validation of IDA4D/SAMI3 and SAMI3 against *in situ* electron density data from CHAMP (~450-km) and Swarm A (~425-km) from 2:25-3:00 UT on 21 November 2003 and 23:15-23:50 UT on 25 August 2018 respectively. The results indicate that IDA4D/SAMI3 performs much better than SAMI3 in reproducing the major features of the independent CHAMP and SWARM *in situ* data.

271 Table 1 shows a statistical comparison of these two passes (covering the same data points
 272 shown in Figure 8). All values are in $10^{10} \text{ el. m}^{-3}$.

| | Bias | RMSE | Max | Min |
|------------------------------|------|------|-----|-----|
| CHAMP (November 2003) | | | | |

| | | | | |
|------------------------------|----|----|-----|------|
| SAMI3 | 22 | 83 | 148 | -160 |
| IDA4D/SAMI3 | 19 | 51 | 130 | -94 |
| Swarm A (August 2018) | | | | |
| SAMI3 | 14 | 23 | 3 | -67 |
| IDA4D/SAMI3 | 0 | 11 | 20 | -31 |

3.3 GPS Validation

The 3D GPS position validation for November 2003 is shown in Figure 9, covering the AMC2 and 1LSU reference stations.

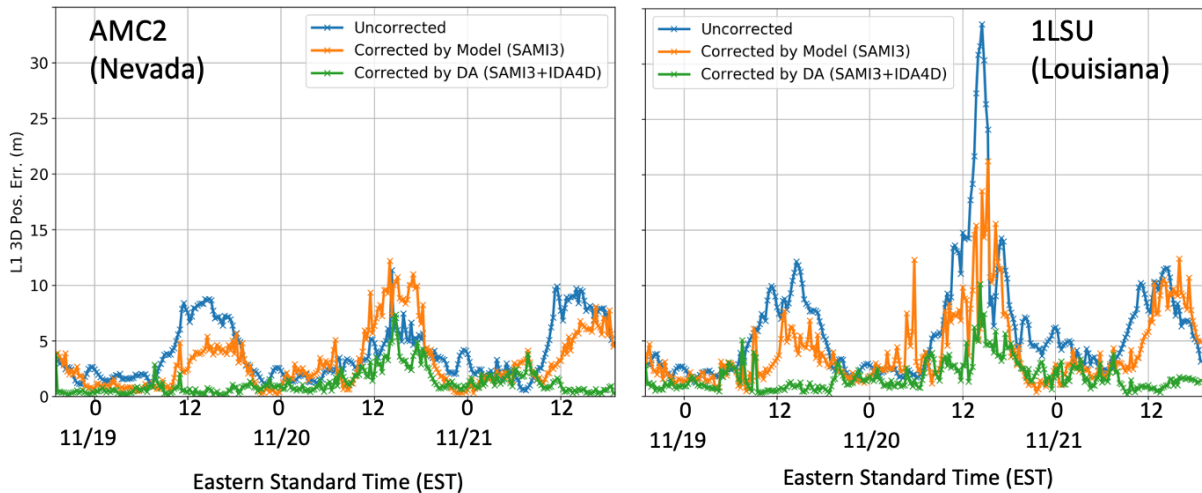


Figure 9: Ionospheric errors on 3D GPS position at AMC2 and 1LSU reference stations, based on uncorrected observed TEC, SAMI3-corrected TEC and IDA4D/SAMI3-corrected TEC.

Uncorrected ionospheric errors on 3D position at the two stations are estimated to have exceeded 34 m in magnitude at 1LSU at the peak of the storm. These errors are reduced to a maximum 10m error at the peak of the storm by IDA4D/SAMI3. Note that the data assimilation is critical to this performance improvement – SAMI3 without data assimilation at best provides only a modest improvement and in some cases makes the positioning solution worse (e.g. at AMC2 on 20 November).

3.4 Ionosonde validation

The ionosonde NmF2 validation shows that data assimilation was effective in correcting the ionospheric state in the November 2003 case. Figure 10 shows a comparison of modeled NmF2 against observations from the WP937 and EG931 digisonde stations (locations shown in Figure 3).

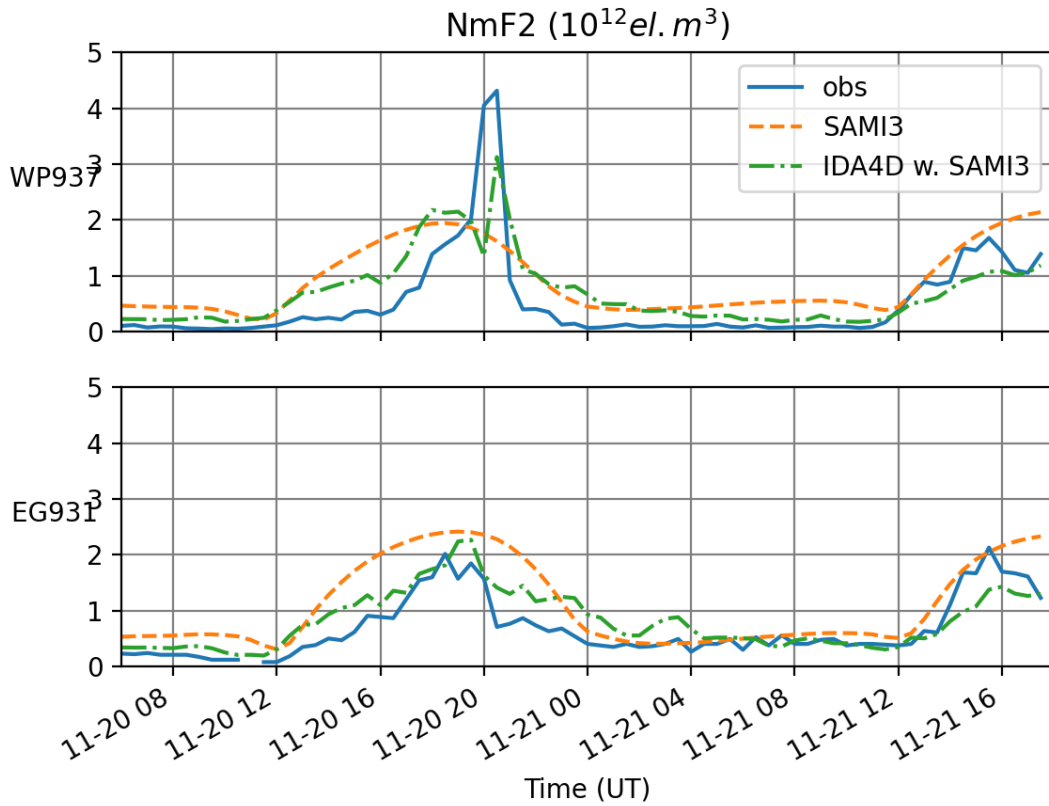


Figure 10 shows a comparison of modeled NmF2 against that observed by ionosondes at WP937 and EG931 stations in the November 2003 case.

The results show that IDA4D is effective in correcting errors in modeled NmF2 during the storm. Statistics are shown in Table 2. The remaining differences may be due either to sub-grid-scale variations, ionogram autoscaling errors or model errors.

Table 2 shows model NmF2 error statistics as compared against autoscaled ionosonde data covering 20-21 November 2003. All values are in 10^{11} el. m^{-3} .

| | Bias | RMSE | Max err. | Min err. |
|--------------|------|------|----------|----------|
| WP937 | | | | |
| SAMI3 | 4 | 8 | 13 | -27 |
| IDA4D/SAMI3 | 2 | 5 | 11 | -27 |
| EG931 | | | | |
| SAMI3 | 4 | 6 | 16 | -1 |
| IDA4D/SAMI3 | 2 | 3 | 1 | -8 |

A similar comparison is performed for the August 2018 case, and is shown in Figure 11. Note that different ionosonde stations were used because of data availability. The results show the same pattern as November 2003, with errors reduced in IDA4D/SAMI3 vs the standalone SAMI3 during the storm.

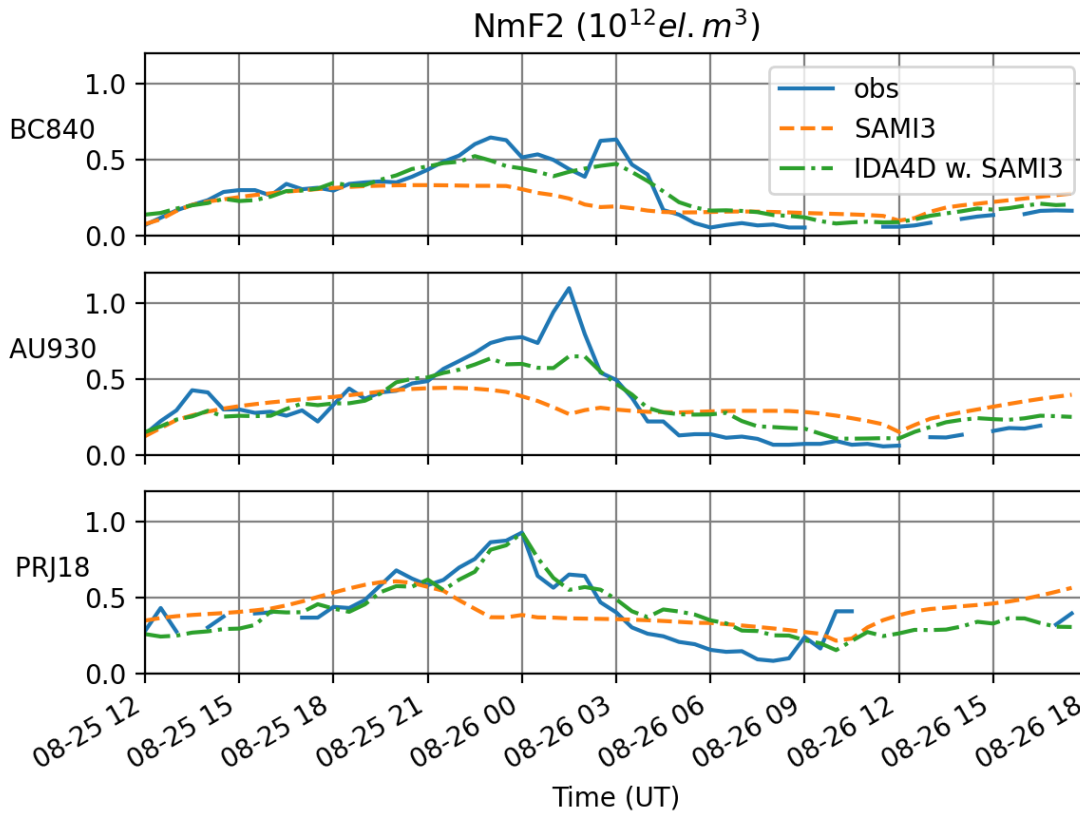


Figure 11 shows a comparison of modeled NmF2 against that observed by digisondes at BC840, AU930 and PRJ18 stations in the August 2018 case.

Table 3 shows model NmF2 error statistics as compared against autoscaled ionosonde data covering 25-26 August 2018. All values are in $10^{11} \text{ el. m}^{-3}$.

| | Bias | RMSE | Max err. | Min err. |
|--------------------|------|------|----------|----------|
| BC840 | | | | |
| SAMI3 | 0 | 2 | 1 | -4 |
| IDA4D/SAMI3 | 0 | 1 | 1 | -2 |
| AU930 | | | | |
| SAMI3 | 0 | 2 | 2 | -8 |
| IDA4D/SAMI3 | 0 | 1 | 2 | -5 |
| PRJ18 | | | | |
| SAMI3 | 0 | 2 | 2 | -5 |

| | | | | |
|-------------|---|---|---|----|
| IDA4D/SAMI3 | 0 | 1 | 2 | -2 |
|-------------|---|---|---|----|

4. Discussion

The new coupled IDA4D/SAMI3 model provides insights into the NILE phenomenon. The results of this new technique show night-time (20-24 LT) ionospheric electron density enhancements between 30-40° N MLAT in the aftermath of a great storm (November 2003) and a strong storm (August 2018). In both cases, the plasma source for these enhancements appears to be the storm-enhanced northern equatorial ionization anomaly crest, though there are some important differences between the two events. Independent validation indicates that the IDA4D/SAMI3 results are reliable.

The NILE appears in the results as a ridgelike enhancement of NmF2 between ~30-40° N, which exists post-sunset in the American sector following geomagnetic storms. In the November 2003 superstorm (shown in Figures 4 and Figure 5), the NILE is a long-lived remnant of a huge enhancement of the northern EIA crest, which itself occurs surprisingly late in local time (between 16-24 UT). NmF2 in the NILE peaks at 1.2×10^{12} at 3 UT on 21 November, following a positive storm phase where NmF2 reached 2×10^{13} in the northern anomaly crest at 21 UT on 20 November. Our analysis of that event opens up at least two further questions. First, how can the EIA enhance so dramatically and so late in local time, with a large part of the enhancement occurring post-sunset? Second, why does only the northernmost part of the EIA crest persist late into the night? The hmF2 plots of Figure 4 indicate extremely high peak heights of around 700 km between the two EIA crests in the late evening, which is consistent with the “superfountain” theory of Tsurutani et al. (2008). This enhancement of the EIA also closely fits the maximum “polarization terminator” region (21 UT, western Atlantic) identified by Foster and Erickson (2013). The hmF2 plots of Figure 5 may provide an explanation as to why the poleward portion of the EIA persists longer and eventually forms the NILE. It appears the most equatorward part of the EIA enhancement is substantially (50-100 km) lower in altitude than the NILE (consistent with upward/poleward transport of plasma from the EIA to the NILE), so experiences faster recombination due to increased collisions with the neutral atmosphere. This effect could be magnified in the aftermath of a geomagnetic storm due to thermal expansion of the neutral atmosphere, though we have no direct evidence of that in this case. Likewise, in the absence of the necessary observations, it is impossible to rule out that these effects are driven by thermospheric wind action rather than by polarization electric fields.

The August 2018 strong storm provides a better-observed and less intense comparison case to the November 2003 superstorm. In this event, the effects of the polarization electric field at the terminator are clearly visible in Figure 7. 5-10° degrees east of the location of the terminator, the isodensity contours of the northern EIA crest align to the terminator, leaving a mid-latitude plasma density enhancement over the central USA. This NILE is far less intense and less extended in longitude than that of November 2003, largely because the storm is much smaller.

Analysis of ionospheric errors on GPS positioning indicates that the main phase of the November 2003 storm could have caused 34-m of error on a single-frequency GPS 3D position estimate at 1LSU (in Louisiana), and that this could have been reduced to 10-m using IDA4D/SAMI3 corrections. By comparison, the NILE effect on positioning accuracy in that case was small at ~5m. Errors were generally much smaller at the Nevada test station, indicating the sensitivity of GPS ionospheric errors to geographic location.

Validation against autoscaled ionosonde NmF2 data indicates the IDA4D data assimilation is effective in reducing biases and random errors present in SAMI3 in both storms. In November 2003, biases are reduced from 4 down to 2×10^{11} el. m⁻³ at both WP937 and EG931 while root-mean-square errors are reduced from 8 down to 5×10^{11} el. m⁻³ and 6 down to 3×10^{11} el. m⁻³. In August 2018, the model is unbiased compared to BC840, AU930 and PRJ18 before and after assimilation, while root-mean-square errors are reduced from 2 down to 1×10^{11} el. m⁻³ at all three stations. In most cases maximum and minimum errors are also reduced or unchanged post-assimilation.

Conclusions

The newly-coupled IDA4D/SAMI3 shows the NILE occurring after storms in November 2003 and August 2018. The phenomenon appears as a moderate, longitudinally extended enhancement of NmF2 at 30-40° N, occurring in the late evening (20-24 LT) following much larger enhancements of the equatorial anomaly crests in the main phase of the storm. Electric field effects related to the “superfountain” and the polarization at the terminator appear to be the cause of these enhancements. Validation against independent *in situ* density data, autoscaled ionosonde NmF2 data and reference GPS data indicates that IDA4D is effective in correcting biases present in SAMI3. The impact can be 35-50% reductions in root-mean-square NmF2 errors, and up to 70% improvement in GPS positioning estimates.

Acknowledgements

The authors acknowledge the support of NASA LWS-TRT grant NNH17ZDA001N-LWS. IDA4D/SAMI3 output is available on Zenodo at: 10.5281/zenodo.4598982. Geophysical indices obtained from NASA OMNI: <https://omniweb.gsfc.nasa.gov/> Ground GPS data obtained from <http://millstonehill.haystack.mit.edu/> courtesy of Anthea Coster. Raw data are available from the International GNSS Service. CHAMP and GRACE data obtained from <https://isdc.gfz-potsdam.de>. Ionosonde data obtained from <http://giro.uml.edu/didbase/scaled.php>. The pyIGRF wrapper was used to generate geomagnetic coordinates: <https://pypi.org/project/pyIGRF/>. Davitpy was used to plot the solar terminator: <https://github.com/vtsuperdarn/davitpy>

References

- Bust, G. S., Garner, T. W., & Gaussiran, T. L. (2004). Ionospheric Data Assimilation Three-Dimensional (IDA3D): A global, multisensor, electron density specification algorithm. *Journal of Geophysical Research: Space Physics*, 109(A11).
- Buonsanto, M. J. (1999). Ionospheric storms—A review. *Space Science Reviews*, 88(3-4), 563-601.
- Collins, N., G. Theurich, C. DeLuca, M. Suarez, A. Trayanov, V. Balaji, P. Li, W. Yang, C. Hill, and A. da Silva (2005). Design and Implementation of Components in the Earth System Modeling Framework. *International Journal of High Performance Computing Applications*, Volume 19, Number 3, pp. 341-350.
- Datta-Barua, S. (2004, September). Ionospheric threats to space-based augmentation system development. In *Proc. ION GNSS 2004* (pp. 21-24).
- Datta-Barua, S., Mannucci, A. J., Walter, T., and Enge, P., "Altitudinal variation of midlatitude localized TEC enhancement from ground- and space-based measurements," *Space Weather*, 6, S10D06, 2008, doi:10.1029/2008SW000396.
- Drob, D. P., Emmert, J. T., Meriwether, J. W., Makela, J. J., Doornbos, E., Conde, M., et al. (2015). An update to the Horizontal Wind Model (HWM): The quiet time thermosphere. *Earth and Space Science*, 2, 301–319. <https://doi.org/10.1002/2014EA000089>
- Fejer, B. G., J. W. Jensen, T. Kikuchi, M. A. Abdu, and J. L. Chau (2007), Equatorial Ionospheric Electric Fields During the November 2004 Magnetic Storm, *J. Geophys. Res.*, 112, A10304, doi:10.1029/2007JA012376.
- Foster, J. C., & Erickson, P. J. (2013). Ionospheric superstorms: Polarization terminator effects in the Atlantic sector. *Journal of Atmospheric and Solar-Terrestrial Physics*, 103, 147-156.
- Fuller-Rowell, T. J. (1998). The "thermospheric spoon": A mechanism for the semiannual density variation. *Journal of Geophysical Research: Space Physics*, 103(A3), 3951-3956.
- Galkin, I. A., Khmyrov, G. M., Kozlov, A. V., Reinisch, B. W., Huang, X., & Paznukhov, V. V. (2008, February). The Artist 5. In *AIP Conference Proceedings* (Vol. 974, No. 1, pp. 150-159). American Institute of Physics.
- Hardy, D. A., Gussenhoven, M. S., & Holeman, E. (1985). A statistical model of auroral electron precipitation. *Journal of Geophysical Research*, 90(A5), 4229–4248.
- Hardy, D. A., Gussenhoven, M. S., & Brautigam, D. (1989). A statistical model of auroral ion precipitation. *Journal of Geophysical Research*, 94(A1), 370–392.

- Huba, J. D., Joyce, G., & Fedder, J. A. (2000). Sami2 is Another Model of the Ionosphere (SAMI2): A new low-latitude ionosphere model. *Journal of Geophysical Research: Space Physics*, 105(A10), 23035-23053.
- Huba, J. D., Joyce, G., Sazykin, S., Wolf, R., & Spiro, R. (2005). Simulation study of penetration electric field effects on the low-to mid-latitude ionosphere. *Geophysical Research Letters*, 32(23).
- Huba, J. D., Joyce, G., & Krall, J. (2008). Three-dimensional equatorial spread F modeling. *Geophysical Research Letters*, 35, L19106. <https://doi.org/10.1029/2009GL040284>
- Huba, J. D., and Sazykin, S. (2014), "Storm time ionosphere and plasmasphere structuring: SAMI3-RCM simulation of the 31 March 2001 geomagnetic storm," *Geophysical Research Letters*, Vol. 41, No. 23, pp. 8208-8214.
- Ippolito, A., Altadill, D., Scotto, C., & Blanch, E. (2018). Oblique Ionograms Automatic Scaling Algorithm OIASA application to the ionograms recorded by Ebro observatory ionosonde. *Journal of Space Weather and Space Climate*, 8, A10.
- Kelley, M. C., B. G. Fejer, and C. A. Gonzales, An explanation for anomalous ionospheric electric fields associated with a northward turning of the interplanetary magnetic field, *Geophys. Res. Lett.*, 6(4), 301-304, 1979.
- Loewe, C. A., & Prolss, G. W. (1997). Classification of mean behavior of magnetic storms. *Journal of Geophysical Research*, 102(A7), 14,209-14,213. <https://doi.org/10.1029/96JA04020>
- Mannucci, A. J., B. T. Tsurutani, B. A. Iijima, A. Komjathy, A. Saito, W. D. Gonzalez, F. L. Guarnieri, J. U. Kozyra, and R. Skoug (2005), Dayside global ionospheric response to the major interplanetary events of October 29 - 30, 2003 "Halloween storms," *Geophys. Res. Lett.*, 32, L12S02, doi:10.1029/2004GL021467
- Picone, J. M., Hedin, A. E., Drob, D. P., & Aikin, A. C. (2002). NRLMSISE-00 empirical model of the atmosphere: Statistical comparisons and scientific issues. *Journal of Geophysical Research*, 107(A12), 1468. <https://doi.org/10.1029/2002JA009430>
- Reigber, Ch, Hermann Lühr, and P. Schwintzer. "CHAMP mission status." *Advances in space research* 30.2 (2002): 129-134.
- Richmond, A.D., (1995). Ionospheric electrodynamics using magnetic apex coordinates. *Journal of geomagnetism and geoelectricity*, 47(2), 191-212.
- Rishbeth, H. (1975). F-region storms and thermospheric circulation. *Journal of Atmospheric and terrestrial physics*, 37(6-7), 1055-1064.

Friis-Christensen, E., Lühr, H., Knudsen, D., & Haagmans, R. (2008). Swarm—an Earth observation mission investigating geospace. *Advances in Space Research*, 41(1), 210-216.

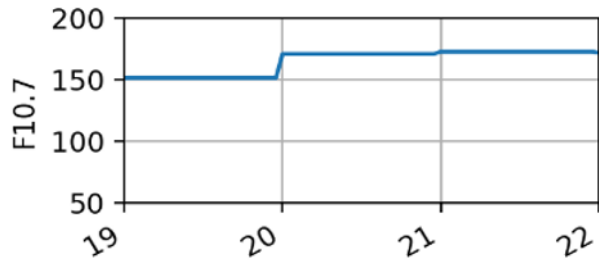
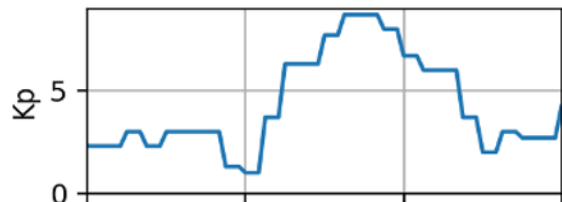
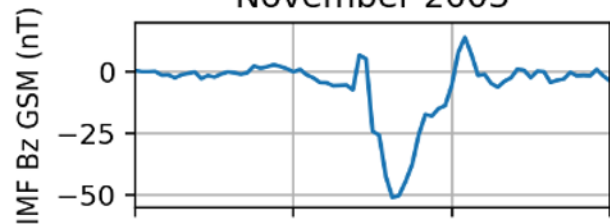
Taeusch, D. R., Carignan, G. R., & Reber, C. A. (1971). Neutral composition variation above 400 kilometers during a magnetic storm. *Journal of Geophysical Research*, 76(34), 8318-8325.

Tsurutani, B. T., Verkhoglyadova, O. P., Mannucci, A. J., Saito, A., Araki, T., Yumoto, K., ... & McCreadie, H. (2008). Prompt penetration electric fields (PPEFs) and their ionospheric effects during the great magnetic storm of 30–31 October 2003. *Journal of Geophysical Research: Space Physics*, 113(A5).

Weimer, D. R. (2005). Predicting surface geomagnetic variations using ionospheric electrodynamic models. *Journal of Geophysical Research*, 110, A12307. <https://doi.org/10.1029/2005JA011270>

Figure 1.

November 2003



August 2018

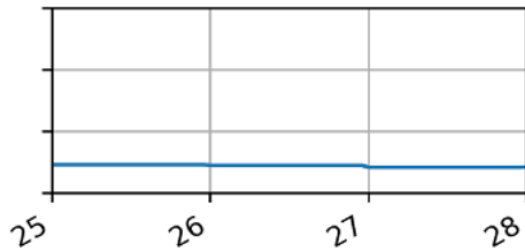
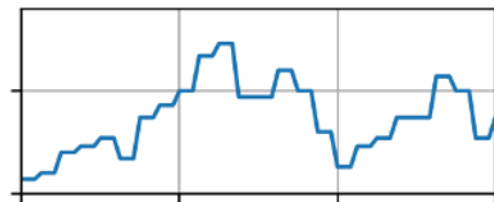
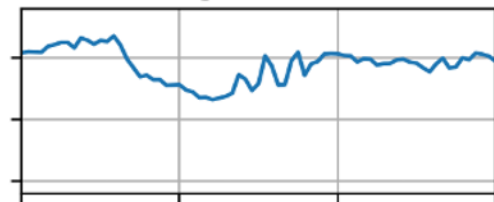


Figure 2.

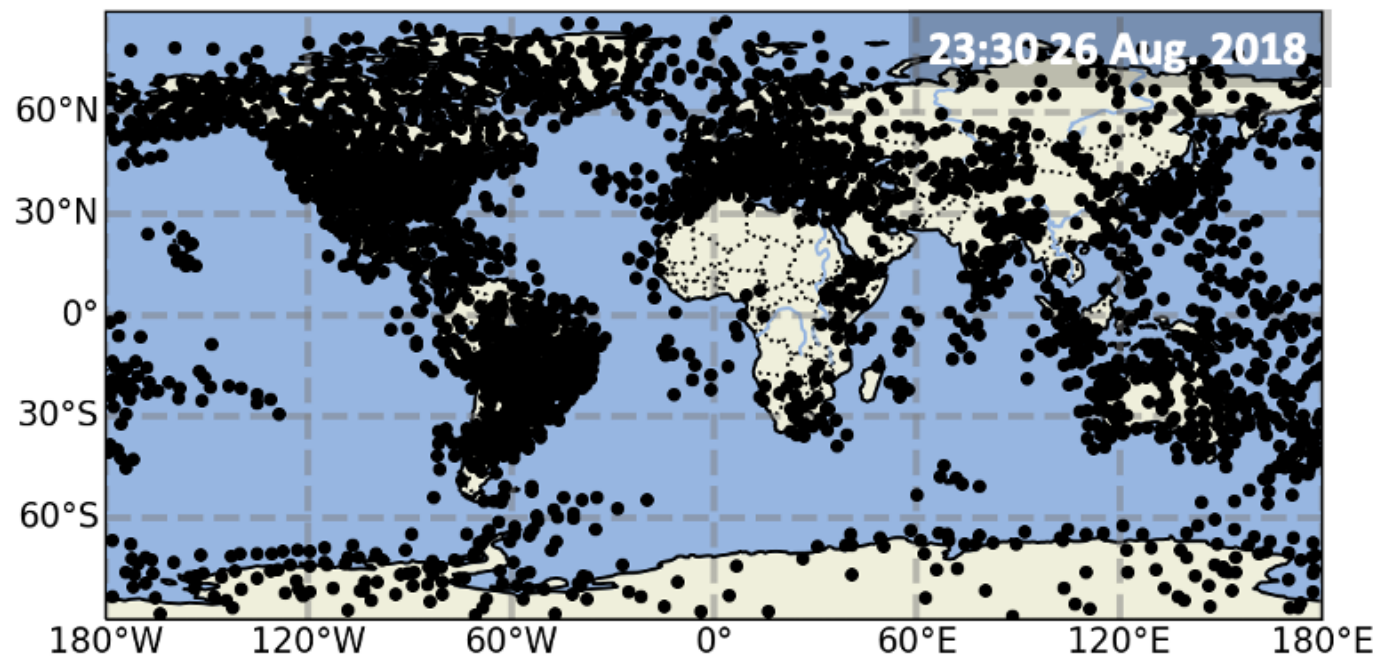
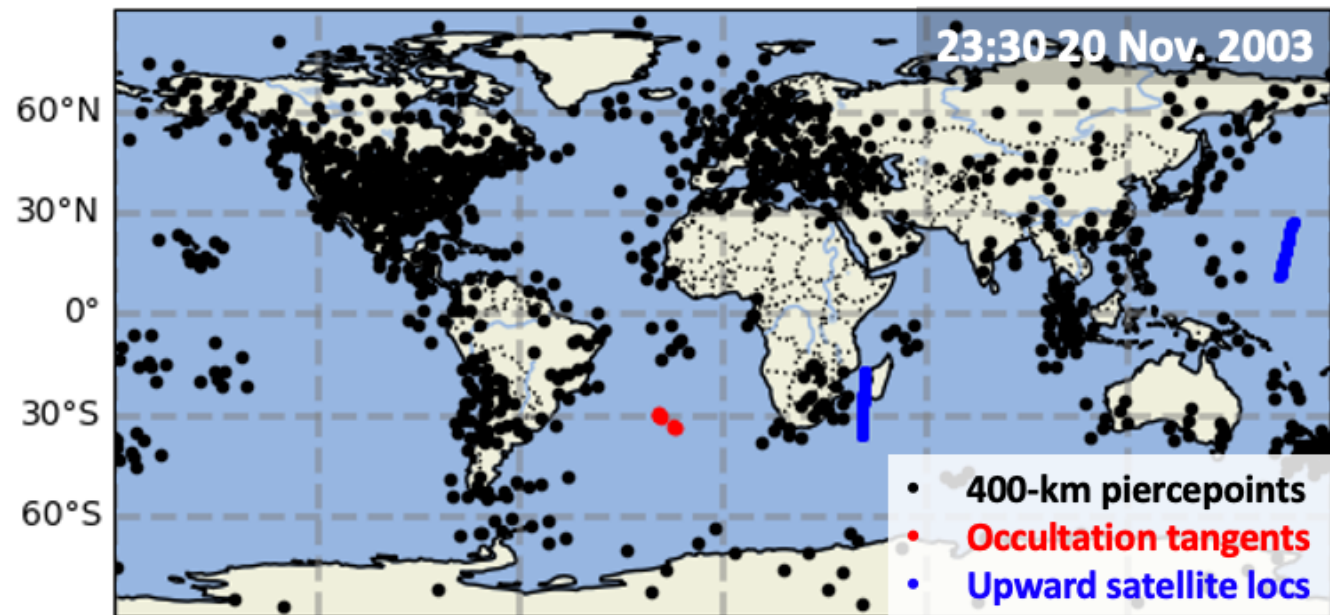


Figure 3.

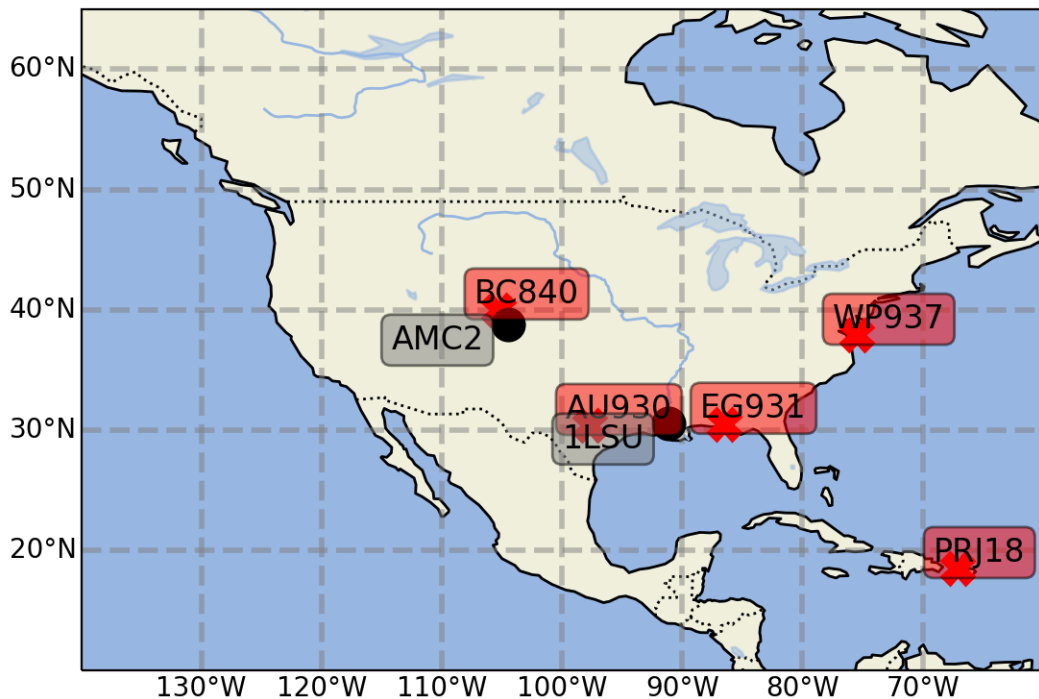
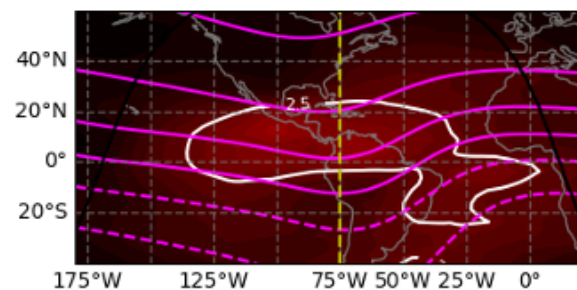
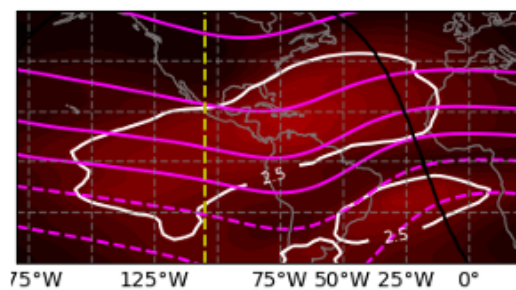


Figure 4.

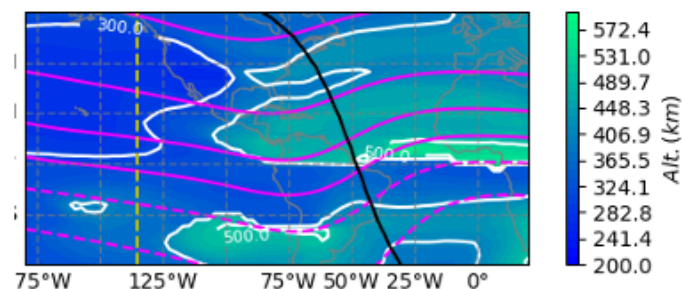
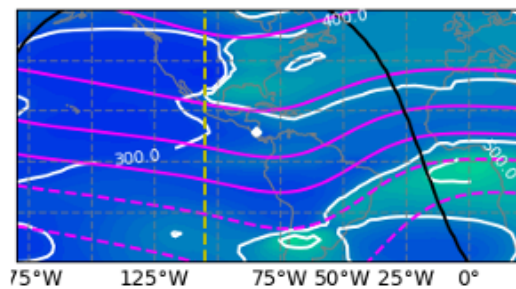
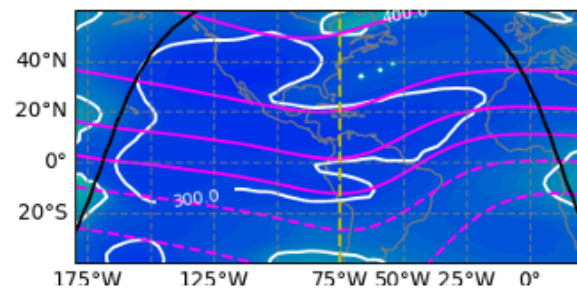
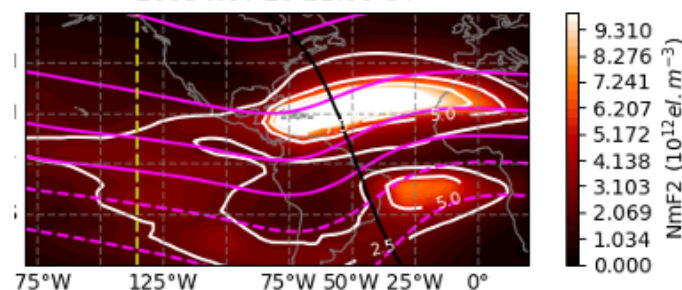
2003 Nov 20 17:00 UT



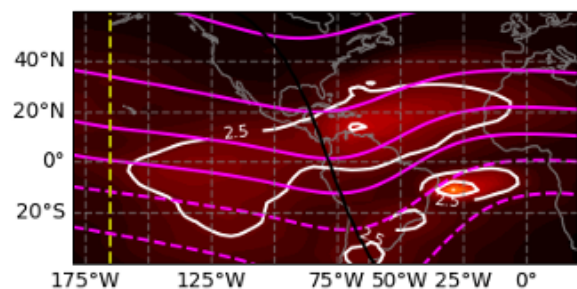
2003 Nov 20 19:00 UT



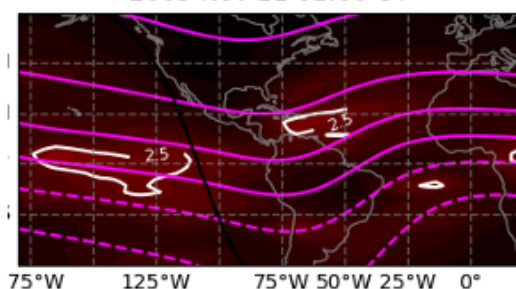
2003 Nov 20 21:00 UT



2003 Nov 20 23:00 UT



2003 Nov 21 01:00 UT



2003 Nov 21 03:00 UT

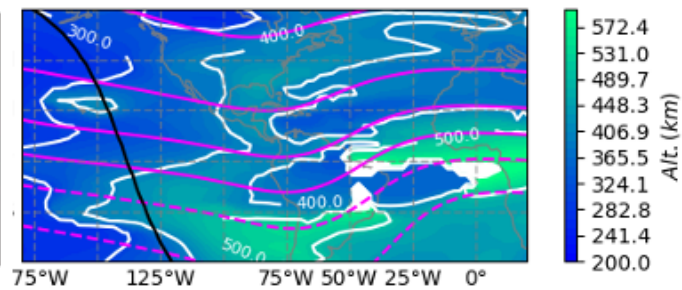
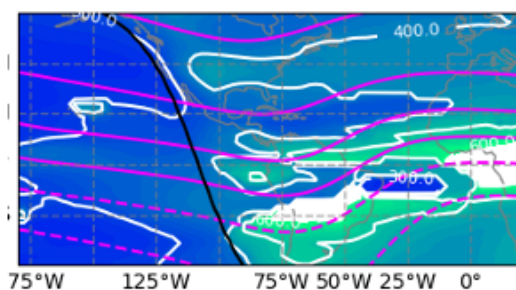
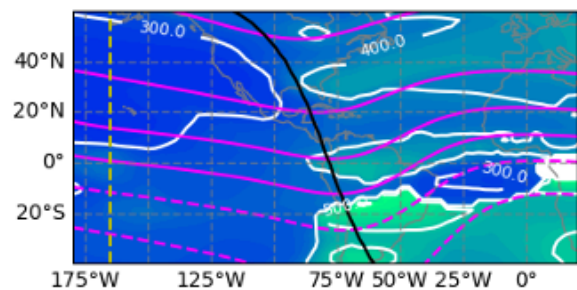
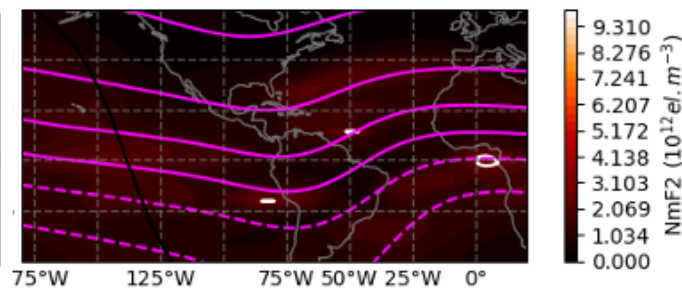
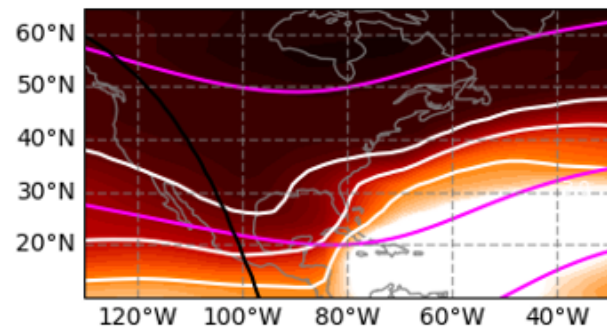
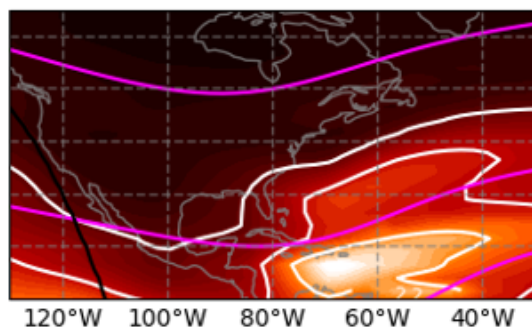


Figure 5.

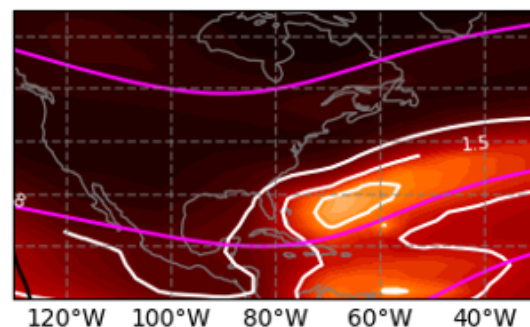
2003 Nov 21 00:00 UT



2003 Nov 21 01:00 UT



2003 Nov 21 02:00 UT



2003 Nov 21 03:00 UT

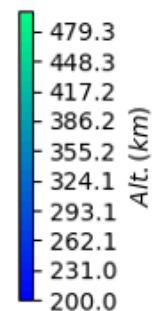
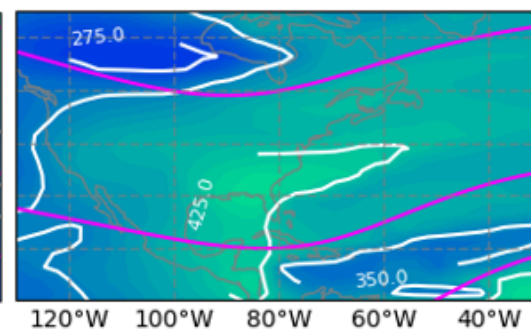
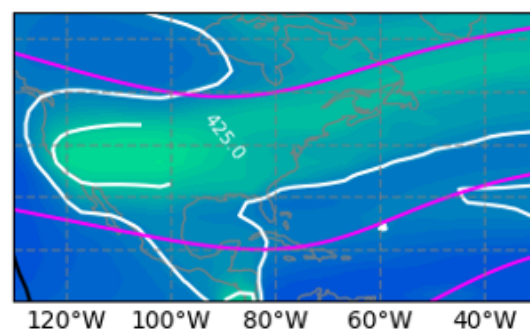
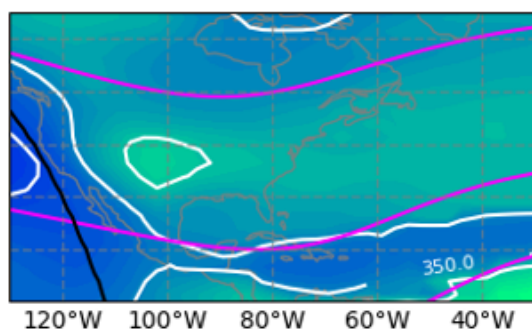
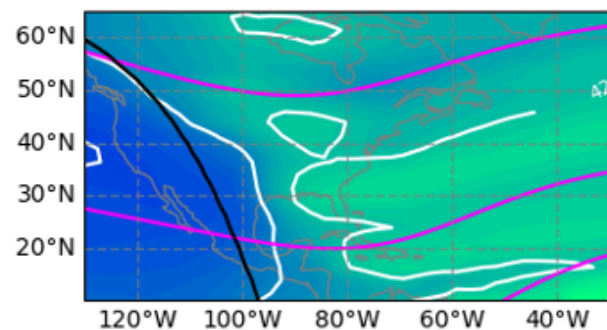
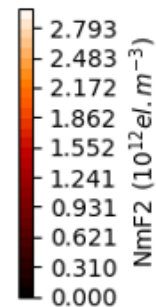
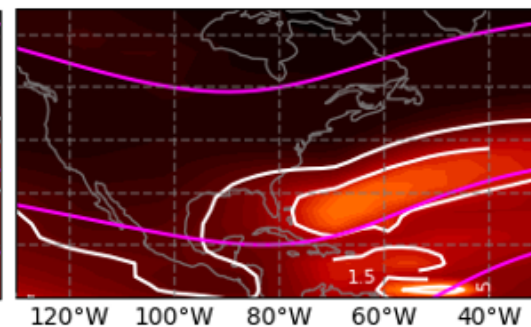
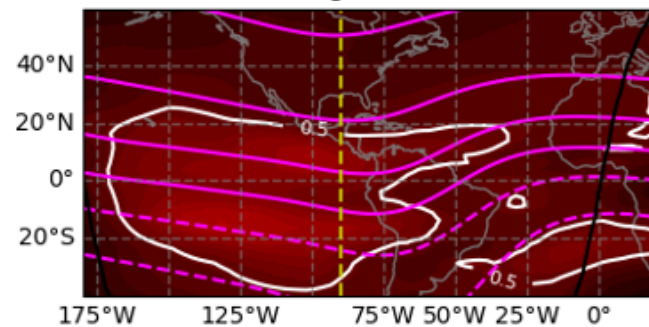
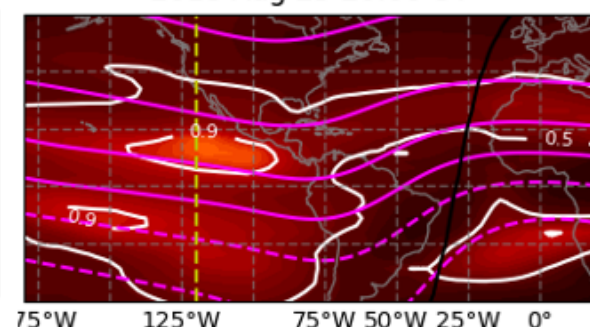


Figure 6.

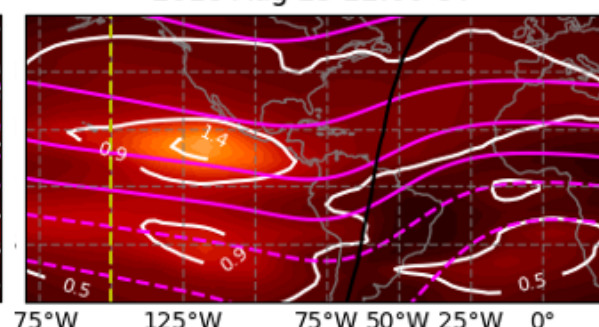
2018 Aug 25 18:00 UT



2018 Aug 25 20:00 UT

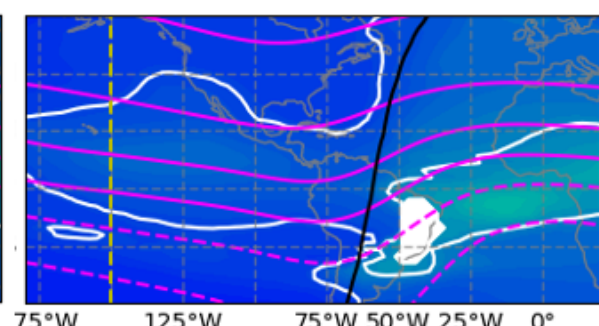
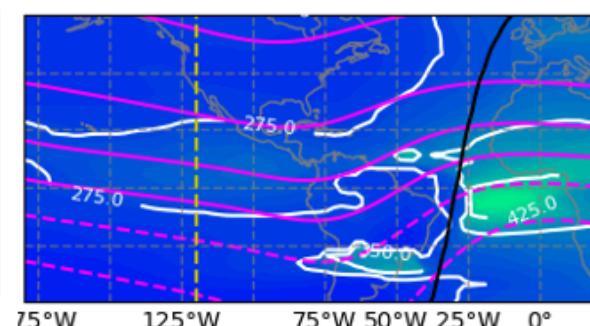
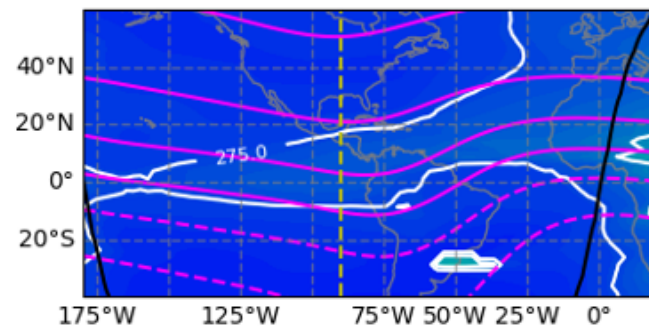


2018 Aug 25 22:00 UT



NmF2 ($10^{12} \text{ el. m}^{-3}$)

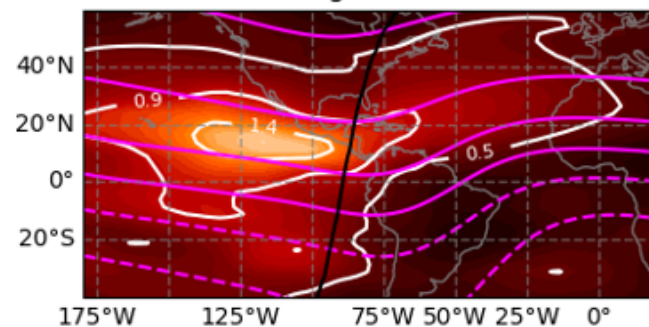
1.676
1.490
1.303
1.117
0.931
0.745
0.559
0.372
0.186
0.000



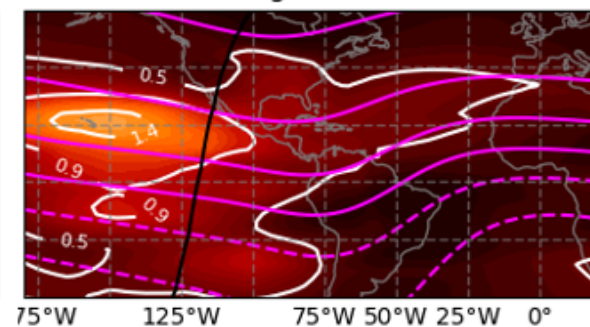
Alt. (km)

479.3
448.3
417.2
386.2
355.2
324.1
293.1
262.1
231.0
200.0

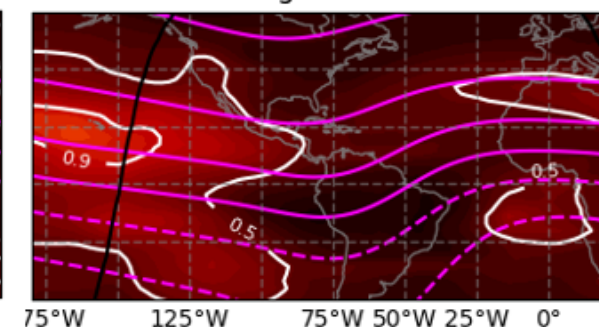
2018 Aug 26 00:00 UT



2018 Aug 26 02:00 UT

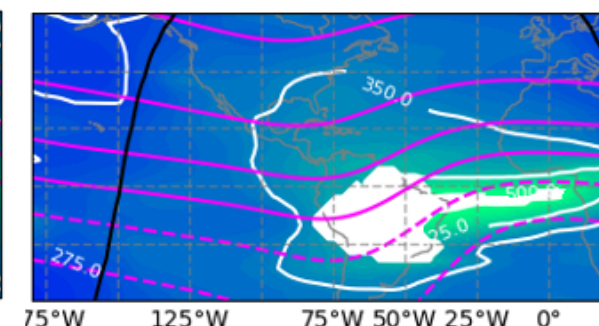
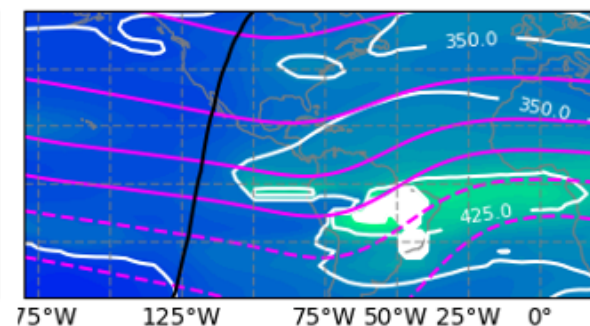
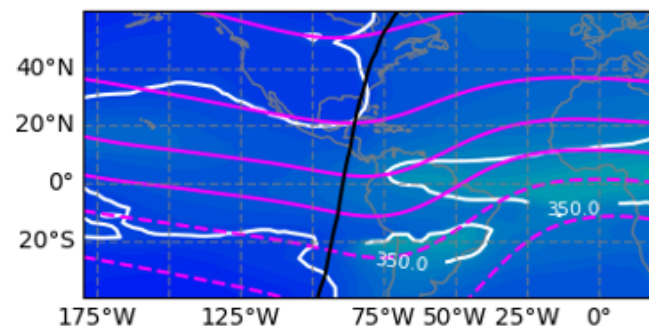


2018 Aug 26 04:00 UT



NmF2 ($10^{12} \text{ el. m}^{-3}$)

1.676
1.490
1.303
1.117
0.931
0.745
0.559
0.372
0.186
0.000



Alt. (km)

479.3
448.3
417.2
386.2
355.2
324.1
293.1
262.1
231.0
200.0

Figure 7.

2018 Aug 26 00:00 UT

2018 Aug 26 01:00 UT

2018 Aug 26 02:00 UT

2018 Aug 26 03:00 UT

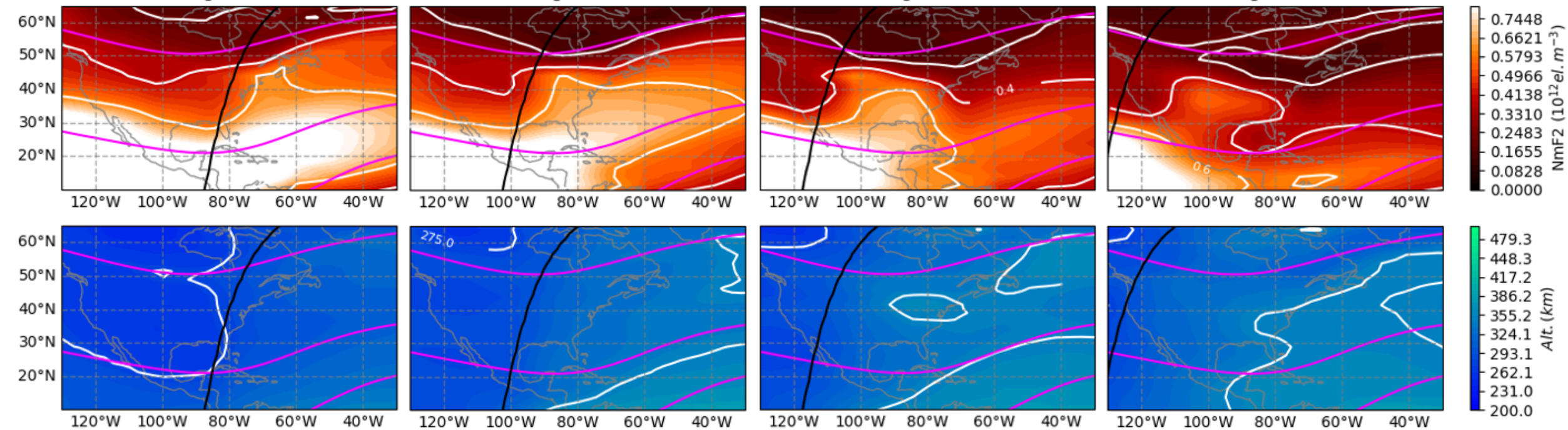


Figure 8.

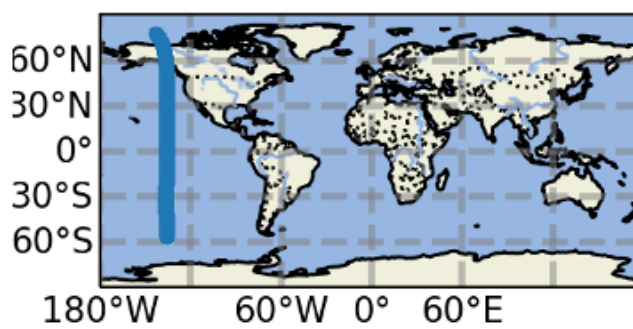
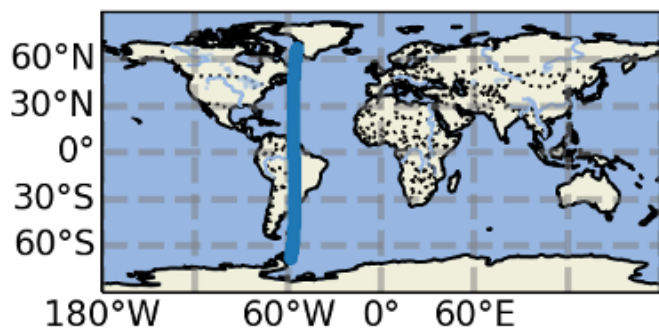
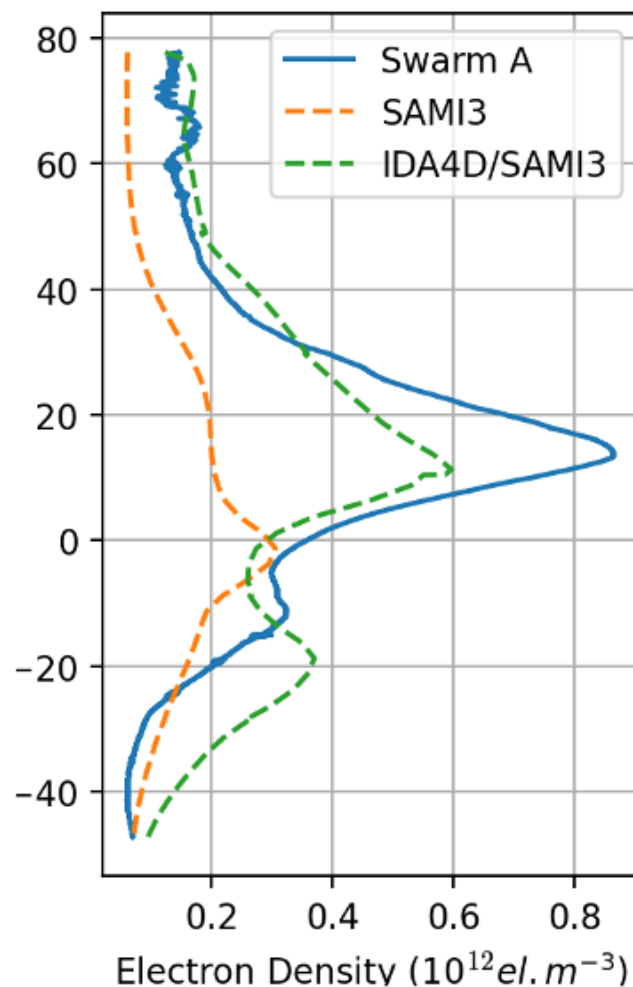
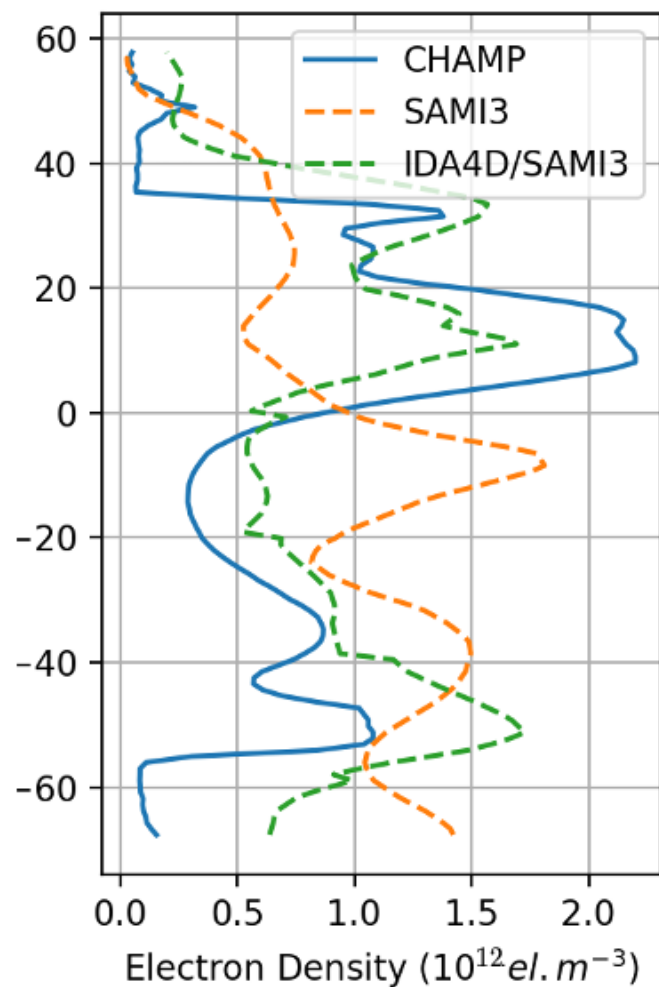


Figure 9.

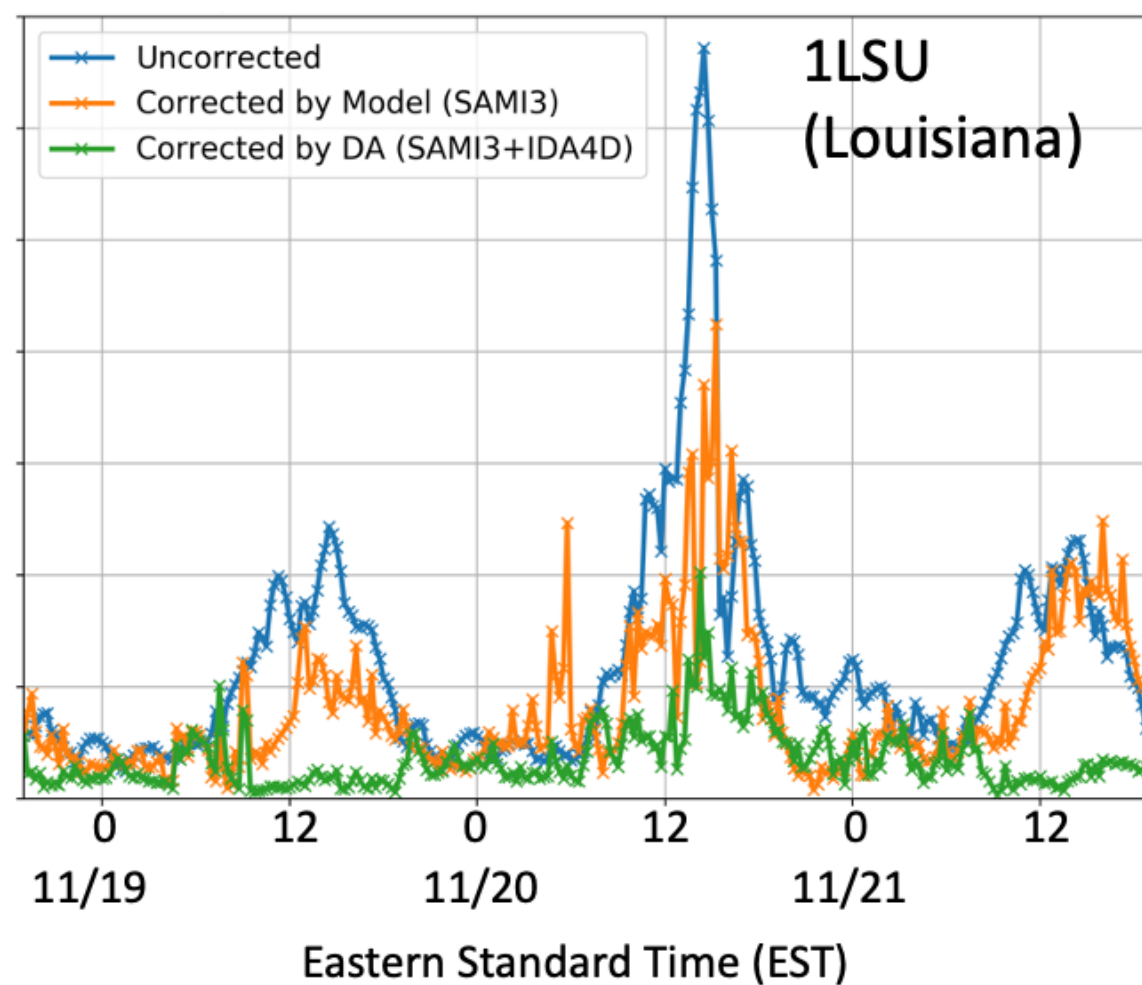
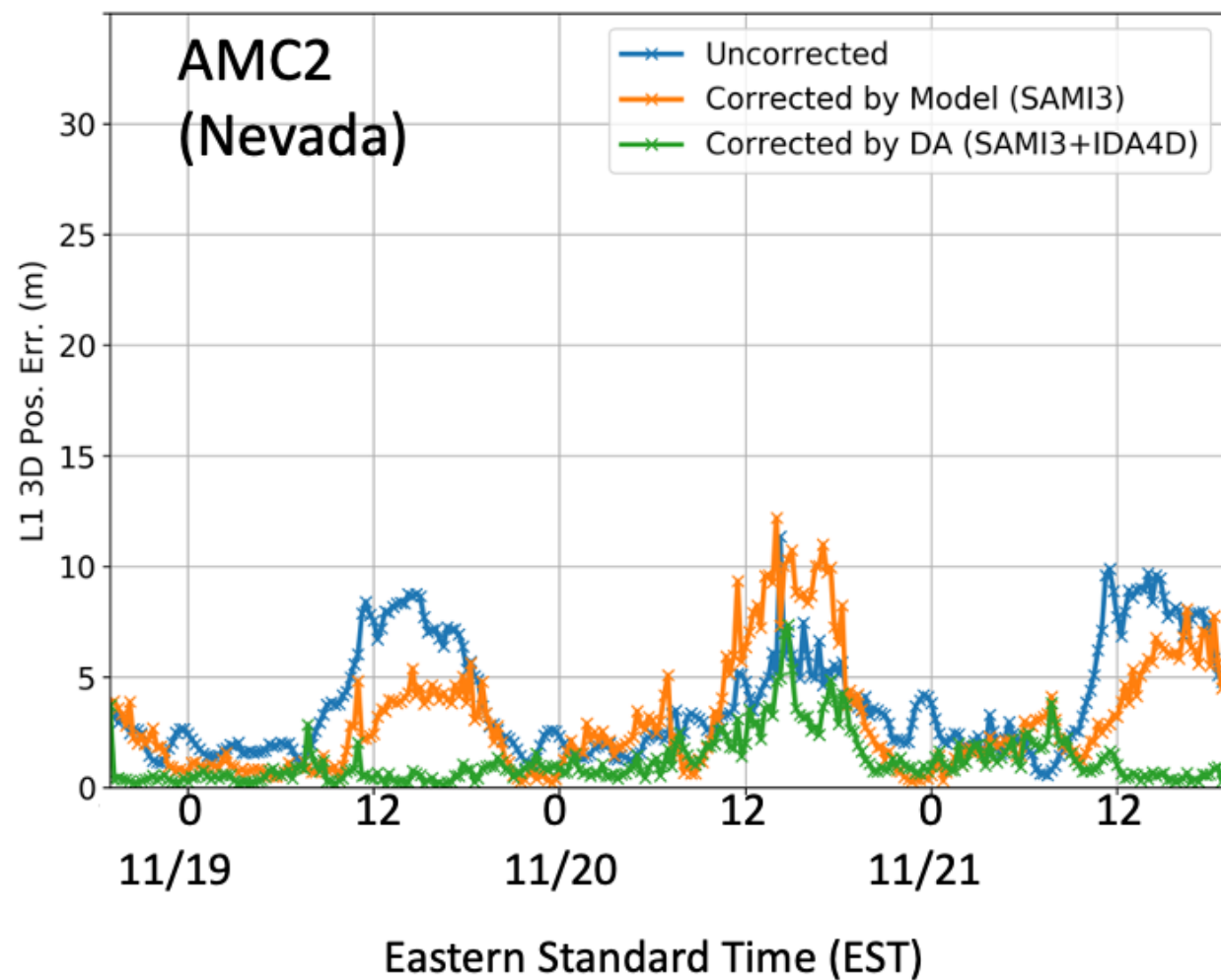


Figure 10.

NmF2 ($10^{12} \text{ el. m}^{-3}$)

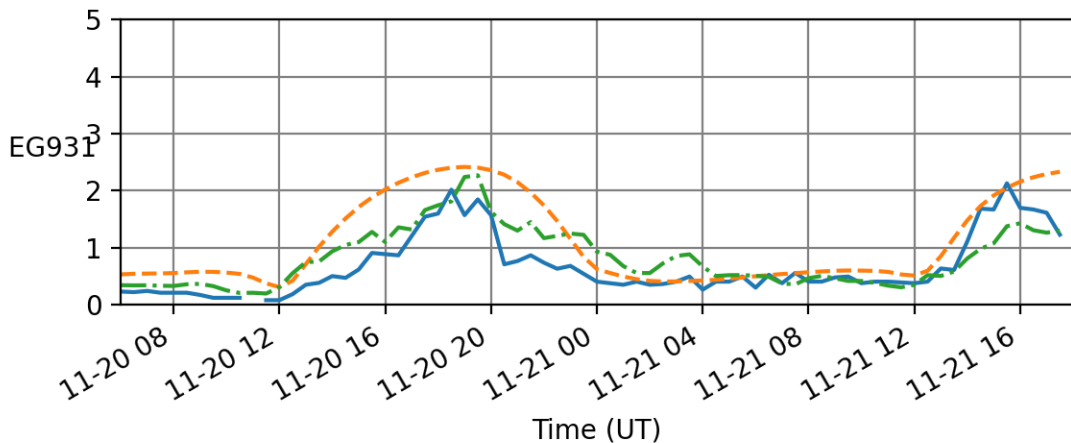
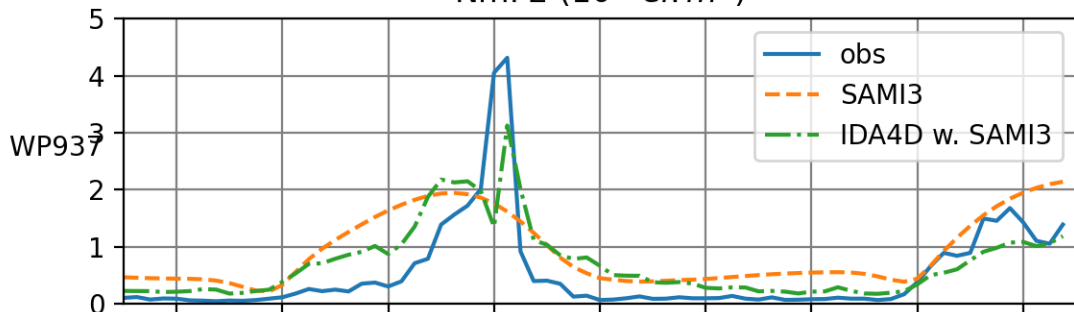


Figure 11.

NmF2 ($10^{12} \text{ el. m}^{-3}$)

